Particle-size segregation in self-channelized granular flows

JM PAPERS

Particle-size segregation in self-channelized granular flows

A.N. Edwards[1], F.M. Rocha[2], B.P. Kokelaar[3], C.G. Johnson[1] and
J.M.N.T. Gray[1],†

[1]Department of Mathematics and Manchester Centre for Nonlinear Dynamics, University of Manchester,
Manchester M13 9PL, UK

[2]Aix Marseille University, CNRS, IUSTI, Marseille 13453, France

[3]Earth and Ocean Sciences Department, University of Liverpool, Liverpool L69 3GP, UK

Geophysical mass flows such as debris flows, dense pyroclastic flows and snow avalanches can self-channelize on shallow slopes. The confinement afforded by formed levees helps to maintain the flow depth, and hence mobility, allowing self-channelized flows to run out significantly farther than unconfined, spreading flows. Levee formation and self-channelization are strongly associated with particle-size segregation, but can also occur in monodisperse flows. This paper uses the monodisperse depth-averaged theory of Rocha *et al.* (*J. Fluid Mech.*, vol. 876, 2019, pp. 591–641), which incorporates a hysteretic friction law and second-order depth-averaged viscous terms. Both of these are vital for the formation of a travelling wave that progressively deposits a pair of levees just behind the front. The three-dimensional velocity field is reconstructed in a frame moving with the front assuming Bagnold flow. This enables a bidisperse particle-size segregation theory to be used to solve for the large and small particle concentrations and particle paths in three-dimensions, for the first time. The model shows that the large particles tend to segregate to the surface of the flow, forming a carapace that extends over the centre of the channel, as well as along the external sides and base of the levee walls. The small particles segregate downwards, and are concentrated in the main channel and in the inner levee walls. This supports the contention that a low-friction channel lining provides a secondary mechanism for run-out enhancement. It is also shown that the entire theory scales with particle diameter, so experiments with millimetre-sized particles provide important insights into geophysical-scale flows with boulders and smaller rock fragments. The model shows that self-channelization does not need particle-size segregation to occur, but supports the hypothesis that particle-size segregation and the associated frictional feedback can significantly enhance both the flow mobility and the levee strength.

† Email address for correspondence: nico.gray@manchester.ac.uk

---

1. Introduction

Debris flows consist of a concentrated mixture of water and rock fragments that range widely in size and tend to segregate during shear (Iverson 1997). Large grains tend to rise to the free surface, while small grains percolate down towards the base (Gray 2018). Since the downslope velocity is greatest at the free surface, large rocks and boulders are preferentially transported to the front, where they are overrun by the bulk flow. As finer grained material is sheared over the top of them, these large particles segregate upwards and are eventually transported forwards, towards the front again, by the bulk flow field. In two-dimensional flows (that are sheared through the flow depth), this process leads to the recirculation and accumulation of large grains at the flow front (Gray & Kokelaar 2010). Since the large rock fragments tend to be more resistive to motion than the finer grained material, the front becomes increasingly resistive and the flow can stop. In three-dimensions, this increased frontal resistance can be alleviated by pushing the large particles out of plane, towards the sides of the flow, to form static levees (Sharp & Nobles 1953; Costa & Williams 1984; Pierson 1986; Iverson 1997; Major 1997; Iverson & Vallance 2001; Félix & Thomas 2004; Johnson *et al.* 2012; Laigle & Bardou 2022). This process generates a self-channelized flow, with a coarse-grained snout and a more mobile, finer-grained flow in the channel which pushes the front downslope. The central channel is bounded on either side by static large-rich levees, as shown schematically in figure 1.

The self-channelization process is important because it prevents lateral spreading, maintaining the flow depth and hence the flow mobility for longer. This can significantly extend the overall run-out distance (Goujon, Dalloz-Dubrujeaud & Thomas 2007; Kokelaar *et al.* 2014). Coarse-fragment-rich debris flows commonly self-channelize as they move on to shallower slopes (Iverson & Vallance 2001; Félix & Thomas 2004; Johnson *et al.* 2012). Figure 2(*a*) shows an example from the bottom of the Biregrabe on the Albristore, near Färmelberg, Switzerland. There is a coarse-grained snout, as well as parallel-sided levees that are almost entirely composed of similar material. The levees are approximately 4 m apart and extend about 217 m upstream on a 10° slope, to where this small flow was diverted out of the main channel. As the flow waned, the central channel drained almost completely, leaving just the levees as evidence of the debris flow's path (figure 2b). Much larger debris flows occurred in this area on the 20 August 2012 and 24 July 2015, due to melting permafrost and high rainfall (C. Berger, personal communication). The deposits shown in figure 2 are interesting because the snout (which is often washed out by subsequent rainfall) has been almost perfectly preserved. It was deposits such as this and other observations of flowing debris flows that inspired Laigle & Bardou (2022) to draw their schematic diagram shown here in figure 1.

Self-channelization also occurs in other geophysical mass flows, such as in the dense basal layer of pyroclastic flows, water-saturated lahars and wet snow avalanches (Rowley, Kuntz & MacLeod 1981; Wilson & Head 1981; Branney & Kokelaar 1992; Calder, Sparks & Gardeweg 2000; Vallance 2000; Jomelli & Bertran 2001; Jessop *et al.* 2012; Ancey 2012; Bartelt *et al.* 2012; Schweizer, Bartelt & Van Herwijnen 2014; Vallance & Iverson 2015). Although these flows contain fluid, which helps to mobilize them, self-channelization is not dependent on the presence of the fluid. Kokelaar *et al.* (2017) identified strongly leveed, fingered rock avalanche deposits in the southeast sector of Bessel crater in Mare Serenitatis on the Moon (see their figure 10). The fronts of
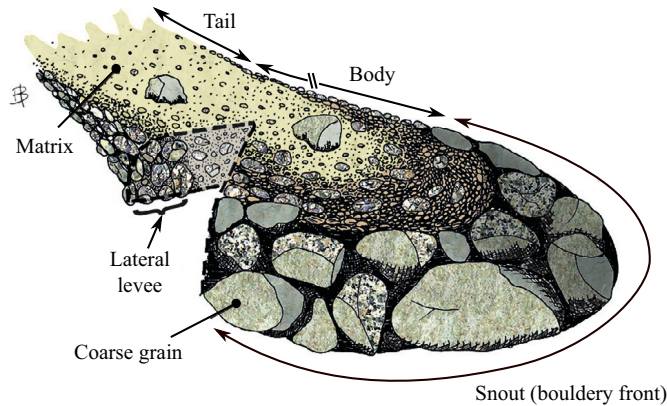
Figure 1. Schematic diagram showing the different parts of a typical debris-flow surge (reproduced from Laigle & Bardou 2022). The flow develops a bouldery snout which is pushed along by the concentrated mixture of water and finer grains behind. There are a wide range of grain sizes within this mixture and larger grains segregate to the surface of the flow. Since the downslope velocity is greatest at the free-surface, there is a continual supply of relatively large fragments to the front, and, rather than accumulating there, these are shouldered aside to form static levees on either side of the central channel. As the flow wanes, the tail of the flow is a less concentrated mixture of finer grains and water that is typically more turbulent. Several surges are generally observed during a single event. The body is longer than appears on the figure (represented by the broken arrow).

these flows came to rest on a $\sim 31.5°$ slope, and all of them look remarkably similar to the Biregrabe deposit in figure 2. These flows occurred in the complete absence of water or atmosphere. Interstitial fluids may therefore modify the frictional properties and significantly enhance the flow's mobility (Iverson & George 2014; Meng, Johnson & Gray 2022), but they are not necessary for a flow to self channelize on a suitably inclined slope.

Félix & Thomas (2004) were able to generate leveed channels in small-scale analogue experiments with monodisperse dry grains. This showed that although particle-size segregation commonly occurs (and may be very important), it is not fundamentally necessary to generate a self-channelized flow. The coexistence of layers of static and flowing grains of similar thickness and at the same inclination angle, led Félix & Thomas (2004) to suggest that self-channelization was related to frictional hysteresis. Frictional hysteresis (Daerr & Douady 1999) is responsible for the effect that when a steady uniform flow is brought to rest on a rough bed, a layer of grains of thickness $h = h_{stop}(\zeta)$ is deposited at a slope angle ζ, but this layer does not start to flow again until the chute is inclined to a higher angle $\zeta_{start}(h) > \zeta$. Pouliquen & Forterre (2002) showed how to capture this phenomenon by defining a non-monotonic basal friction law in a depth-averaged avalanche model. This friction law had (i) a multivalued static regime, (ii) a monotonically decreasing intermediate regime and (iii) a monotonically increasing dynamic regime, as a function of Froude number over the flow thickness. This friction law allowed static and flowing states to coexist for thicknesses in the range $h \in [h_{stop}(\zeta), h_{start}(\zeta)]$, where $h_{start}(\zeta)$ is the inverse function of $\zeta_{start}(h)$.

Mangeney *et al.* (2007) incorporated Pouliquen & Forterre's (2002) friction law into a depth-averaged avalanche model, and solved the system of equations numerically to show that it could generate a self-channelized flow with static levees. However, it was unclear what selected the width and height of the ensuing channel, which had multiple steady-state solutions. This contradicted the experimental evidence, which shows that for a given mass flux there is a well-defined channel width and height
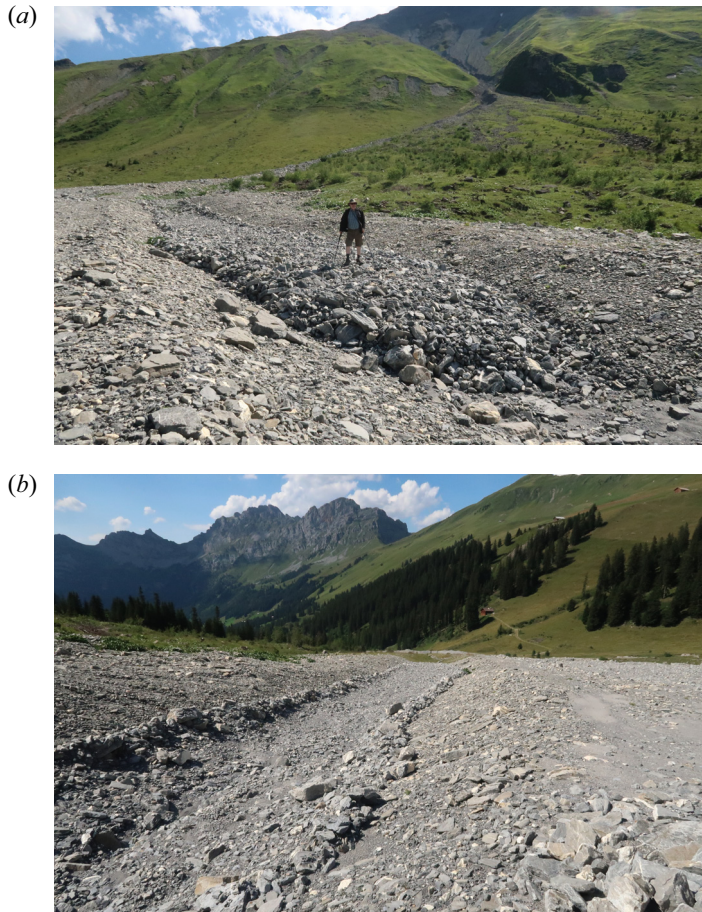
(*a*)

(*b*)

Figure 2. (*a*) Self-channelized flow front deposited at the bottom of the Biregrabe on the Albristore, near Färmelberg, Switzerland (latitude 46°30′43.43" N, longitude 7°29′40.17" E, elevation 1775 m, slope ∼10°). This area experienced large debris flows on the 20 August 2012 and 24 July 2015 due to melting permafrost and high rainfall (C. Berger, personal communication). This smaller deposit formed between 2017 and 2018. (*b*) Parallel-sided levees (approximately 4 m apart) left stranded at the side of the central channel as the flow waned.

(Félix & Thomas 2004; Deboeuf *et al.* 2006; Takagi, McElwaine & Huppert 2011; Rocha, Johnson & Gray 2019). This conundrum was solved by Rocha *et al.* (2019), who incorporated additional depth-averaged in-plane viscous terms (Gray & Edwards 2014; Baker, Barker & Gray 2016*a*), which generate a downslope velocity profile across the central channel. This provides the missing length scale that selects the steady-state flow height and the channel width. Rocha *et al.* (2019) showed that the resulting model was able to quantitatively capture experimental measurements of flow height and channel width as a function of the mass flux for quasi-monodisperse (0.45 ± 0.15 mm) dry sand (Félix & Thomas 2004; Takagi *et al.* 2011). Moreover, at low mass fluxes, Rocha *et al.* (2019) also correctly showed that self-channelized flows become unstable, and break down into a series of 'erosion–deposition' waves (Takagi *et al.* 2011; Edwards & Gray 2015; Edwards *et al.* 2017, 2019). Similar surge waves that progressively erode and deposit previously fluidized material along their path are also commonly observed in debris flows (McArdell 2016).

955 A38-4

The dynamic part of the non-monotonic friction law is intimately linked to the $\mu(I)$ rheology for dry granular flows (GDR-Midi 2004; Jop, Forterre & Pouliquen 2005, 2006; Gray & Edwards 2014; Baker *et al.* 2016a). Rather than having a constant Coulomb friction, the $\mu(I)$ rheology introduces rate dependence by making the friction μ a function of the inertial number

$$I = \frac{\dot{\gamma} d}{\sqrt{p/\rho_*}}, \tag{1.1}$$

where $\dot{\gamma}$ is the shear rate, d is the particle diameter, p is the granular pressure and ρ_* is the intrinsic density of the grains. This has spawned intense interest in the rheology of dry granular flows, as it provides a promising way of modelling chute flows, column collapses, silos and flows in rotating drums (GDR-Midi 2004; Jop *et al.* 2006; Lagrée, Staron & Popinet 2011; Staron, Lagrée & Popinet 2012; Barker *et al.* 2015; Barker & Gray 2017; Martin *et al.* 2017; Schaeffer *et al.* 2019; Barker *et al.* 2021). The $\mu(I)$ rheology does not, however, capture the formation of h_{stop} or h_{start} layers. This phenomenology appears to be a non-local effect in which the ability of grains to flow, or not, is affected by motion some distance away (Schall & Van Hecke 2010). In the case of h_{stop} and h_{start} layers, it is the proximity of the fixed basal boundary to the free surface that has a strong effect on the ability of the grains to remain stable. An alternative approach (to the depth-averaged one used in this paper) is therefore to use one of the non-local models for granular flow (Pouliquen & Forterre 2009; Kamrin & Koval 2012; Bouzid *et al.* 2013, 2015; Kamrin & Henann 2015). In particular, Mowlavi & Kamrin (2021) have recently captured both the h_{stop}, h_{start} phenomenology in one-dimensional time-dependent simulations with a non-local model that includes hysteresis. Applying such models in three dimensions to capture self-channelization and levee formation remains, however, a significant challenge for the future.

If the relatively simple monodisperse depth-averaged model of Rocha *et al.* (2019) can quantitatively capture the self-channelization process, one may reasonably ask: (i) what is the role of particle segregation and (ii) does the small-scale experimental evidence have any bearing on large-scale geophysical flows? Interestingly, the strongly leveed, fingered rock avalanche deposits that Kokelaar *et al.* (2017) identified in the Bessel crater, look almost identical to small-scale segregation induced fingering experiments of Pouliquen, Delour & Savage (1997), Woodhouse *et al.* (2012) and Baker, Johnson & Gray (2016b). This led Kokelaar *et al.* (2017) to develop a scaling argument to show that the depth-averaged system of equations used by Baker *et al.* (2016b) (which is similar to the model of Rocha *et al.* (2019), but includes the depth-averaged effect of segregation) scales with gravity g and a typical grain diameter d. Large-scale segregating bouldery dry flows on the Moon are therefore closely similar to small-scale dry flows with millimetre-sized particles on Earth.

In geophysical flows, the range of particle sizes is very wide, with particle diameters varying by several orders of magnitude. This allows particles to pack much more densely than monodisperse flows even during shear, which reduces the rate of segregation, and can lead to intermediate and reverse segregation for very large intruders (Thomas 2000). Such effects not only introduce bulk compressibility, but are still well beyond the scope of current granular rheologies and polydisperse particle-size segregation models (Gray & Ancey 2011; Marks, Rognon & Einav 2012; Gray 2018; Barker *et al.* 2021). Indeed, until recently the segregation and diffusion rates in bidisperse segregation models (even with relatively small grains-size ratios) were poorly constrained (Golick & Daniels 2009; Thornton *et al.* 2012; Fan *et al.* 2014; Hill & Tan 2014; Schlick *et al.* 2015; van der Vaart *et al.* 2015; Fry *et al.* 2019). As one of the first papers to investigate particle segregation

in a non-trivial three-dimensional flow field, this paper uses a simple bidisperse model with the empirical segregation law of Trewhela, Ancey & Gray (2021). Trewhela *et al.* (2021) used refractive-index-matched shear-box experiments to track the segregation of large and small intruders as a function of time, and determined a scaling law that could collapse all their data. For grain-size ratios close to unity, they found that the segregation velocity magnitude is linearly dependent on the shear rate, the intrinsic particle density, the gravitational acceleration, the square of the average grain diameter and the deviation of the grain-size ratio away from unity, and inversely proportional to the pressure. Additional corrections, which are necessary at moderate grain-size ratios when the percolation of small intruders can be enhanced due to the spontaneous percolation, are ignored here, as are enhanced packing effects at large size ratios.

The inclusion of interstitial fluid also introduces additional complexity. For example, differentially fluidized regions of the flow will produce differential friction, which provides another mechanism to generate self-channelization without invoking frictional hysteresis. In particular, drier coarse-grained flow fronts and lateral levees will experience more friction than the fluid-saturated channel (Sharp & Nobles 1953; Wilson & Head 1981; Costa & Williams 1984; Iverson & Vallance 2001; Iverson 2003). This inhomogeneous rheology may well prove to be crucial at geophysical scale. In general, mixtures of grains and water can form suspensions whose friction $\mu = \mu(J)$ is dependent on the viscous inertial number $J = \eta_f \dot{\gamma}/p^p$, where η_f is the fluid viscosity and p^p is the particle pressure (Boyer, Guazzelli & Pouliquen 2011). This constitutive law is valid for slow flows or small non-colloidal particles. As the shear rate is increased, the flow can transition from viscous inertial to granular inertial regimes with the friction $\mu = \mu(K)$, where $K = J + \alpha I^2$ is a combination of the viscous and granular inertial numbers and α is a constant, approximately equal to 0.1 (Tapia *et al.* 2022). The ratio $I^2/J = \rho_* d^2 \dot{\gamma}/\eta_f$ defines a Stokes number St, which is particle-size dependent, and governs the extent to which the particles are affected by the fluid. If $St \gg 1/\alpha$, then the particles are affected by fluid buoyancy, but do not closely follow fluid streamlines and in dense flows, they are in the inertial granular regime (Maurin, Chauchat & Frey 2016). Particles with $St \ll 1/\alpha$ are strongly affected by the fluid and are in the viscous inertial regime. For debris flows, where there is a wide range of grain sizes, it is likely that the rocks and coarse-grained sand are in the inertial granular regime, while the very finest grains will be in the viscous inertial regime. The implicit assumption in this paper is that the larger grains dominate the overall debris-flow response, and hence the $\mu(I)$ rheology is most appropriate (GDR-Midi 2004; Jop *et al.* 2006; Gray & Edwards 2014).

In depth-averaged two-phase-flow models, the primary effect of the fluid is the buoyancy-induced reduction in the granular friction, which may additionally be enhanced by excess pore-pressure effects (Iverson & Denlinger 2001; Pitman & Le 2005; Pelanti, Bouchut & Mangeney 2008; Pudasaini 2012; Iverson & George 2014; Meng & Wang 2016; Meng *et al.* 2022). These allow debris flows to propagate over much shallower slopes than dry granular materials, as in the debris flow at Färmelberg (figure 2). However, on these shallower slopes, the resulting flow dynamics and observed deposit morphologies are closely similar to the dry small-scale experiments (Sharp & Nobles 1953; Wilson & Head 1981; Costa & Williams 1984; Branney & Kokelaar 1992; Iverson 1997; Major 1997; Major & Iverson 1999; Calder *et al.* 2000; Iverson & Vallance 2001; Iverson 2003; Félix & Thomas 2004; Iverson *et al.* 2010; Takagi *et al.* 2011; Johnson *et al.* 2012; Kokelaar *et al.* 2014; Rocha *et al.* 2019).

The aim of this paper is to study the segregation in a representative three-dimensional self-channelizing flow field (Rocha *et al.* 2019). A specific example is chosen which scales

up (Kokelaar *et al.* 2017) to look qualitatively similar to the large-scale experimental debris flows at the United States Geological Survey (USGS) flume (Iverson *et al.* 2010; Johnson *et al.* 2012). This flow field therefore provides a generic test case. In § 2, the depth-averaged theory of Rocha *et al.* (2019) is introduced, and this is used in § 3 to compute a two-dimensional travelling wave solution for the process of self-channelization. In § 4, incompressibility and assumed velocity profiles are used to reconstruct a realistic flow field for self-channelization in three dimensions. This flow field is then held fixed for the remainder of the paper.

Our study is motivated by the USGS debris-flow experiments (Johnson *et al.* 2012) and the experiments of Kokelaar *et al.* (2014), which both had quite tightly constrained particle-size distributions. In the bidisperse small-scale experiments, Kokelaar *et al.* (2014) used mixtures of glass ballotini and carborundum, and glass ballotini and sand, with size ratios of approximately 1.81 and 1.63, respectively. The flume experiments had a more realistic continuous grain-size distribution ranging from 100 μm to 32 mm, but the most pronounced segregation occurred between grains of modest size ratio (<5). Kokelaar *et al.* (2014) used a resin impregnation and sectioning technique to reveal the internal particle-size distribution within the levees and the central channel. The levees were not entirely composed of large grains, as one might anticipate from surface observations, but had an inner core of fine grains. Fine grains also line the inside of the channel. Experimental measurements of the run-out distance as a function of flow composition led Kokelaar *et al.* (2014) to infer that it was the formation of levees and a fine particle channel lining that led to the maximum run out with 60–70 % fines. This was first because the $\mu(I)$ rheology implies that a finer-grained flow experiences less friction (for grains of the same shape), and can flow further and faster, than a larger grained flow of the same depth (GDR-Midi 2004; Rognon *et al.* 2007; Barker *et al.* 2021), and second because lateral confinement maintains flow depth, and hence mobility, for longer. Flows of pure fine grains at the same slope angle do not self-channelize, instead spreading laterally and stopping more rapidly (Kokelaar *et al.* 2014). In debris flows and pyroclastic flows, fine grains additionally hinder the escape of water and gas, and thereby help to maintain high pore pressures, which also convey mobility to the flow (Iverson 2003). The particle-size distribution can therefore have a profound effect on the bulk flow behaviour, and this paper seeks to understand how it develops in the three-dimensional self-channelizing flow field developed in § 4. In § 5, a state-of-the-art particle segregation model (Gray 2018; Barker *et al.* 2021) is introduced that uses Trewhela *et al.*'s (2021) empirical segregation law. Fully three-dimensional, time-dependent, numerical solutions for the particle-size distribution in the vicinity of the moving front are then computed in § 6. The dependence on the grain-size ratio and the inflow concentration are investigated in § 7, and § 8 concludes.

2. Depth-averaged model for self-channelization

2.1. *Governing equations*

Granular material is supplied from a point source onto a rough plane that is inclined at an angle ζ to the horizontal. A Cartesian coordinate system $Oxyz$ is defined with the origin O located at the top centre of the plane. The x-axis points downslope, the y-axis points across the slope and the z-axis is the upward pointing normal. The unit normals are $\boldsymbol{e}_x$, $\boldsymbol{e}_y$ and $\boldsymbol{e}_z$, and the velocity $\boldsymbol{u}$ has components (u, v, w) in each of these three directions, respectively. The equations are integrated through the flow depth h, measured normal to the plane, and

the depth-averaged velocity $\bar{\boldsymbol{u}}$ has components

$$\bar{u} = \frac{1}{h} \int_0^h u \, dz, \quad \bar{v} = \frac{1}{h} \int_0^h v \, dz, \quad (2.1a,b)$$

in the downslope and cross-slope directions, respectively. The granular material is assumed to be incompressible with a constant-uniform bulk density ρ. It follows that the depth-averaged mass and momentum balance equations (Gray & Edwards 2014; Baker *et al.* 2016*a*; Edwards *et al.* 2017) are

$$\frac{\partial h}{\partial t} + \text{div} \, (h\bar{\boldsymbol{u}}) = 0, \quad (2.2)$$

$$\frac{\partial}{\partial t} \, (h\bar{\boldsymbol{u}}) + \text{div} \, (h\bar{\boldsymbol{u}} \otimes \bar{\boldsymbol{u}}) + \text{grad} \left(\frac{1}{2} h^2 g \cos \zeta \right) = hg\boldsymbol{S} \cos \zeta + \text{div} \left(\nu h^{3/2} \bar{\boldsymbol{D}} \right), \quad (2.3)$$

where $\otimes$ is the dyadic product and g is the constant of gravitational acceleration. Note that the two-dimensional divergence and gradient operators, div and grad, are used here to distinguish them from their three-dimensional counterparts, which are written in terms of the ∇ operator in §5. In the source term on the right-hand side of (2.3), the non-dimensional net acceleration,

$$\boldsymbol{S} = \tan \zeta \, \boldsymbol{e_x} - \mu_b \boldsymbol{e}, \quad (2.4)$$

consists of the component of gravity pulling the avalanche downslope along the direction of the unit vector $\boldsymbol{e_x}$ and the effective basal friction μ_b. The hysteretic effective basal friction law for μ_b is introduced in §2.2. It is a generalization of Pouliquen's (1999*a*) dynamic friction law, which is directly linked to the $\mu(I)$ rheology for granular flows (GDR-Midi 2004; Jop *et al.* 2005, 2006; Gray & Edwards 2014; Baker *et al.* 2016*a*). If the avalanche is in motion, the direction of the friction, $\boldsymbol{e}$, opposes the motion, and when the grains are static, the friction opposes the downslope component of gravitational acceleration and the depth-averaged pressure gradient, which implies that

$$\boldsymbol{e} = \begin{cases} \dfrac{\bar{\boldsymbol{u}}}{|\bar{\boldsymbol{u}}|} & \text{if } |\bar{\boldsymbol{u}}| > 0, \\[4mm] \dfrac{\tan \zeta \, \boldsymbol{e_x} - \text{grad} \, h}{|\tan \zeta \, \boldsymbol{e_x} - \text{grad} \, h|} & \text{if } |\bar{\boldsymbol{u}}| = 0. \end{cases} \quad (2.5)$$

The final term on the right-hand side of (2.3) arises from the inclusion of depth-averaged in-plane deviatoric stresses, which are neglected in most theories. Here, however, they play a crucial role in selecting a unique solution for the steady-state channel width and height. Gray & Edwards (2014) and Baker *et al.* (2016*a*) derived the specific form for this second-order-gradient depth-averaged viscous term from the $\mu(I)$ rheology. It consists of a depth-averaged viscosity $\nu h^{1/2}/2$ that multiplies the depth-integrated strain-rate tensor

$$\bar{\boldsymbol{D}} = \tfrac{1}{2} \left(\bar{\boldsymbol{L}} + \bar{\boldsymbol{L}}^T \right), \quad (2.6)$$

where $\bar{\boldsymbol{L}} = \text{grad} \, \bar{\boldsymbol{u}}$ is the two-dimensional gradient of the depth-averaged velocity. The coefficient ν is determined from the $\mu(I)$ friction law (GDR-Midi 2004; Jop *et al.* 2006) and an explicit formula will be given for it in §2.3.

2.2. *The hysteretic friction law*

This paper uses the hysteretic friction law of Edwards *et al.* (2019), which is a generalization of Pouliquen & Forterre's (2002) original law. It consists of three cases that are known as the dynamic, intermediate and static friction regimes

$$
\mu_b(h/d, Fr) = \begin{cases} \mu_D, & Fr \geqslant \beta_*, \\ \mu_I, & 0 < Fr \leqslant \beta_*, \\ \mu_S, & Fr = 0. \end{cases} \tag{2.7}
$$

These regimes are defined respectively by the functions

$$
\mu_D = \mu_1 + \frac{\mu_2 - \mu_1}{1 + h\beta/(\mathcal{L}d(Fr + \Gamma))}, \tag{2.8}
$$

$$
\mu_I = \left(\frac{Fr}{\beta_*}\right)\left(\mu_1 + \frac{\mu_2 - \mu_1}{1 + h\beta/(\mathcal{L}d(\beta_* + \Gamma))} - \mu_3 - \frac{\mu_2 - \mu_1}{1 + h/(\mathcal{L}d)}\right) + \mu_3 + \frac{\mu_2 - \mu_1}{1 + h/(\mathcal{L}d)}, \tag{2.9}
$$

$$
\mu_S = \min\left(\mu_3 + \frac{\mu_2 - \mu_1}{1 + h/(\mathcal{L}d)}, \, |\tan\zeta \, \boldsymbol{e}_x - \operatorname{grad} h|\right), \tag{2.10}
$$

where $\mu_1 = \tan\zeta_1$, $\mu_2 = \tan\zeta_2$ and $\mu_3 = \tan\zeta_3$ are the tangents of the friction angles ζ_1, ζ_2 and ζ_3. These parameters are determined from experimental fits to the deposit depth $h_{stop}(\zeta)$ and initiation thickness $h_{start}(\zeta)$ as a function of ζ. The fitting functions contain a frictional length scale $\mathcal{L}$, which Forterre & Pouliquen (2003) showed scales with the grain size d. This grain-size dependence has explicitly been included in (2.8)–(2.10) by defining the non-dimensional friction length scale $\mathcal{L} = \mathcal{L}/d$. The regime boundaries are determined by the Froude number Fr, which is the ratio of the flow speed to the gravity wave speed

$$
Fr = \frac{|\bar{\boldsymbol{u}}|}{\sqrt{gh\cos\zeta}}. \tag{2.11}
$$

If Fr is above the minimum Froude number β_* for steady-uniform flow, then the flow is in the dynamic regime, if the Froude number equals zero, it is in the static regime and if $Fr \in (0, \beta_*)$, then it is in the intermediate regime. The remaining non-dimensional constants β and Γ are determined from a pair of best fits to the steady-uniform-flow law for angular particles (Forterre & Pouliquen 2003)

$$
Fr = \beta\frac{h}{h_{stop}} - \Gamma. \tag{2.12}
$$

Edwards *et al.* (2019) assumed that the minimum observable steady-uniform flow occurs at the same Froude number $Fr = \beta_*$ at all slope angles. It follows from (2.12) that the minimum steady-uniform-flow depth

$$
h_* = \left(\frac{\beta_* + \Gamma}{\beta}\right)h_{stop}(\zeta), \tag{2.13}
$$

which implies that h_* is a multiple of h_{stop}. The frictional parameters must be chosen so that $h_{stop} < h_* < h_{start}$ for the hysteretic friction law to be well defined. A necessary, but not sufficient condition is that $\mu_1 < \mu_3 < \mu_2$. This paper adopts the parameters for sand used by Rocha *et al.* (2019), except for ζ_3, which is increased from $31°$ to $33°$. This increases the maximum static friction and hence the thickness range ($h \in [h_{stop}, h_{start}]$)

ζ_1	ζ_2	ζ_3	$\mathcal{L}$	β	Γ	β_*	d	ρ	g
$29.0°$	$45.5°$	$33.0°$	2	0.71	0.84	0.11	0.45 mm	1500 kg m^{-3}	9.81 m s^{-2}

Table 1. Material properties for flows of sand with a mean diameter of 0.45 mm. The values of ζ_1, ζ_2 and $\mathcal{L}$ were calculated from the h_{stop} curve of Takagi *et al.* (2011) by Rocha *et al.* (2019). The values of β and Γ differ from those in Pouliquen & Forterre (2002) and Forterre & Pouliquen (2003) to account for the factor $\sqrt{\cos \zeta}$ in the Froude number (2.11). All the values are the same as those used by Rocha *et al.* (2019) except for ζ_3, which is increased from $31°$ to $33°$ to give the sand slightly more stability in the hysteretic flow regime.

with coexisting flowing and static states. Increasing μ_3 gives the levees slightly greater stability than in the simulations of Rocha *et al.* (2019), which suppresses the periodically upslope propagating erosion-deposition waves seen in their movie 5. All the parameters (see table 1) are tightly constrained by existing experiments in the literature and are typical of those for sand flowing on a bed of glass beads. Rocha *et al.* (2019) also gave parameters for flows of glass beads, which also form levees even though $\Gamma = 0$ (Félix & Thomas 2004). The values of μ_1 and μ_3 are, however, very close to one another, which leads to weak non-monotonic dependence of the friction μ on the Froude number Fr, as shown in figure 6(b) of Rocha *et al.* (2019). This leads to very weak levees. Indeed, Deboeuf *et al.* (2006) have observed experimentally that levees of glass beads slowly creep outwards over very long periods of time, which is not the case for sand.

2.3. *The coefficient ν*

Gray & Edwards (2014) and Baker *et al.* (2016a) derived the depth-averaged viscous terms in (2.3) from the $\mu(I)$ rheology (GDR-Midi 2004; Jop *et al.* 2006). In this equation, the coefficient

$$\nu = \frac{2}{9} \frac{\mathcal{L}d\sqrt{g}}{\beta} \frac{\sin \zeta}{\sqrt{\cos \zeta}} \left(\frac{\mu_2 - \tan \zeta}{\tan \zeta - \mu_1} \right), \tag{2.14}$$

is explicitly determined during the integration process in terms of the existing friction parameters, summarized in table 1, and the slope angle ζ. Equation (2.14) is valid for slope inclinations in the range $\zeta \in [\zeta_1, \zeta_2]$, when steady-uniform flows are predicted to exist by the dynamic frictional law (2.8). In reality, the lowest observable steady-uniform flow occurs at $Fr = \beta_*$ and one might anticipate that the form of ν might change when the flow is in the intermediate (2.9) and static (2.10) regimes. However, in the computations presented in this paper, (2.14) is assumed to apply to all regimes.

2.4. *Particle size and gravitational dependence*

The governing equations can be made non-dimensional by introducing scalings based on a typical particle diameter d and gravity g

$$\left. \begin{array}{l} (x, y, z, h) = d\,(\tilde{x}, \tilde{y}, \tilde{z}, \tilde{h}), \quad t = \sqrt{d/g}\,\tilde{t}, \\ \bar{\boldsymbol{u}} = \sqrt{gd}\,\tilde{\bar{\boldsymbol{u}}}, \quad \bar{\boldsymbol{D}} = \sqrt{g/d}\,\tilde{\bar{\boldsymbol{D}}}, \quad \nu = d\sqrt{g}\,\tilde{\nu}, \end{array} \right\} \tag{2.15a–e}$$

where the tilde is used to indicate a non-dimensional variable. It follows that the non-dimensional form of the mass and momentum balances (2.2) and (2.3) are

$$\frac{\partial \tilde{h}}{\partial \tilde{t}} + \widetilde{\text{div}}\left(\tilde{h}\tilde{\bar{\boldsymbol{u}}}\right) = 0, \tag{2.16}$$

$$\frac{\partial}{\partial \tilde{t}}\left(\tilde{h}\tilde{\bar{\boldsymbol{u}}}\right) + \widetilde{\text{div}}\left(\tilde{h}\tilde{\bar{\boldsymbol{u}}} \otimes \tilde{\bar{\boldsymbol{u}}}\right) + \widetilde{\text{grad}}\left(\frac{1}{2}\tilde{h}^2 \cos \zeta\right) = \tilde{h}\boldsymbol{S}\cos \zeta + \widetilde{\text{div}}\left(\tilde{\nu}\tilde{h}^{3/2}\tilde{\bar{\boldsymbol{D}}}\right), \tag{2.17}$$

respectively, where $\widetilde{\text{div}}$ and $\widetilde{\text{grad}}$ are the non-dimensionalized divergence and gradient operators and the non-dimensional coefficient in the viscous term

$$\tilde{\nu} = \frac{2}{9}\frac{\mathcal{L}}{\beta}\frac{\sin \zeta}{\sqrt{\cos \zeta}}\left(\frac{\mu_2 - \tan \zeta}{\tan \zeta - \mu_1}\right). \tag{2.18}$$

Moreover, the non-dimensional net acceleration $\boldsymbol{S}$, the unit vector $\boldsymbol{e}$ and the friction μ_b, defined in (2.4), (2.5) and (2.7), respectively, are already written in dimensionless form, since $\bar{\boldsymbol{u}}/|\bar{\boldsymbol{u}}| = \tilde{\bar{\boldsymbol{u}}}/|\tilde{\bar{\boldsymbol{u}}}|$, grad $h = \widetilde{\text{grad}}\,\tilde{h}$ and $\mu_b(h/d, Fr) = \mu_b(\tilde{h}, Fr)$. The non-dimensional system of equations is therefore independent of any additional non-dimensional groups involving d or g dependence. These non-dimensionalized equations are therefore scale and gravity independent. This remarkable result is due to Kokelaar *et al.* (2017), and implies that provided all the length scales (height, width and length) scale up with the particle size, the results will be the same. A self-channelized geophysical flow of large boulders, such as that shown in figure 2, may therefore be exactly equivalent to a small-scale experimental flow involving millimetre-sized grains (Rocha *et al.* 2019). This scaling on the particle size relies on the fact that the frictional length scale $\mathcal{L} = \mathcal{L}d$ scales linearly on d. Forterre & Pouliquen (2003) showed that $\mathcal{L} = 1.65d$ for glass beads and $\mathcal{L} = 2.03d$ for sand. In this paper, the non-dimensional frictional length $\mathcal{L} = \mathcal{L}/d$ is assumed to be equal to 2 (table 1).

Kokelaar *et al.* (2017) applied these ideas to large-scale dry granular flows on the Moon, which occur during crater wall collapses. The reduced gravity on the Moon implies that the velocities will be slower than an equivalent sized flow on Earth and the flows would therefore have taken correspondingly longer to run out. However, Kokelaar *et al.*'s (2017) figure 10 shows self-channelized fingered deposits in the Bessel crater in Mare Serenitatis (latitude 21.8°N, longitude 17.9°E) that are closely analogous to the small-scale segregation induced fingering experiments of Pouliquen *et al.* (1997), Woodhouse *et al.* (2012) and Baker *et al.* (2016*b*). The presence of water in debris flows on Earth modifies the friction law and the scaling properties. However, the essential flow dynamics and morphological features remain closely similar as demonstrated by the USGS debris-flow-flume experiments (Johnson *et al.* 2012).

3. Depth-averaged simulations of a self-channelized flow

The governing equations in §2 are now solved numerically to generate thickness and depth-averaged velocity fields that quantitatively capture the small-scale self-channelized flow experiments of Takagi *et al.* (2011) and Rocha *et al.* (2019). The scaling behaviour with particle size (see §2.4) ensures that this solution is also appropriate for geophysical flows, whose average grain size is much larger than that in the small-scale experiments. The solution is then transformed to a frame of reference moving with the flow front, to show that over longer integration periods, a travelling-wave solution develops that is steady in the moving frame.

h_{stop}	h_*	h_{start}	ν
5.0 mm	6.7 mm	undefined	2.8×10^{-3} m$^{3/2}$ s^{-1}

Table 2. Critical layer thicknesses h_{stop}, h_* and h_{start} as well as the coefficient ν (in the depth-averaged viscosity $\nu h^{1/2}/2$) for the material properties for sand in table 1 and the fixed slope angle of $\zeta = 32.0°$ used in the numerical computations.

3.1. *Continuous release of grains on an inclined plane*

A numerical simulation is first performed to capture the continuous release of sand from a point source onto a rough plane inclined at $\zeta = 32°$. The values of the critical thicknesses h_{stop}, h_* and h_{start} as well as ν are therefore constant, and their specific values are summarized in table 2. The computational domain consists of a rectangle covering the area 0 m $\leqslant x \leqslant 2.5$ m and -10 cm $\leqslant y \leqslant 10$ cm, discretized to 2500×200 finite volume cells (1 grid point per mm in both directions). The conservation equations (2.2) and (2.3) are solved numerically with a semi-discrete non-oscillatory central (NOC) scheme, which uses a generalized minmod limiter with $\theta = 2$ (Kurganov & Tadmor 2000). The time-stepping is performed with a second-order Runge–Kutta method, with the step size determined by a CFL (Courant–Friedrichs–Lewy) number of 0.225 and limited to a maximum of $\Delta t = 10^{-4}$ s (LeVeque 2002) to minimize the creep in the levees.

The initial conditions at $t = 0$ are $h = h_0 = 0.01$ mm (around 50 times smaller than the mean particle diameter) and $\bar{\boldsymbol{u}} = \mathbf{0}$ m s^{-1} everywhere. This thin static layer is required to mitigate numerical errors caused by the degeneracy of the governing equations at $h = 0$. Following Rocha *et al.* (2019), a source term S_{inflow} is included on the right-hand side of (2.2) to give

$$\frac{\partial h}{\partial t} + \operatorname{div}(h\bar{\boldsymbol{u}}) = S_{inflow}, \tag{3.1}$$

which allows grains to be added in a small circular region of radius $r_0 = 2.5$ cm centred at $(x_0, y_0) = (15$ cm$, 0)$ at a flow rate of $Q_m = 130$ g s^{-1}, i.e.

$$S_{inflow} = \begin{cases} \dfrac{3Q_M}{\pi \rho r_0^6} \left(r_0^2 - \left((x - x_0)^2 + y^2 \right) \right)^2, & (x - x_0)^2 + y^2 \leqslant r_0^2, \\ 0, & (x - x_0)^2 + y^2 > r_0^2. \end{cases} \tag{3.2}$$

The inflowing particles move downslope and some of them eventually reach the downstream boundary $x = 2.5$ m, where a free outflow condition is imposed by linear extrapolation of the values of h and $h\bar{u}$ from the final two columns of interior cells. The conditions $h = h_0$ and $\bar{\boldsymbol{u}} = \mathbf{0}$ m s^{-1} are trivially satisfied at the top $x = 0$ and sides $y = \pm 10$ cm of the domain where no flow reaches.

The results of this numerical simulation are plotted in figure 3 at times $t = 7$, 14, 21 and 28 s. The continuous release of grains is shown to quickly form a self-channelized flow with static levees. In the central flowing channel, which is of approximately constant thickness 9 mm and uniform width 16 cm, material is transported towards the flow front. When it reaches the front, the lateral confinement is lost and the flow spreads out, rapidly coming to rest and building up new sections of the levees just behind the flow front. The levees are approximately 2.5 cm wide and have a thickness that starts at the flowing channel depth and decreases to zero. As a result, the front in figure 3 appears to propagate steadily downslope at constant velocity $u_F \simeq 0.07$ m s^{-1}, suggesting that a two-dimensional travelling wave is generated.
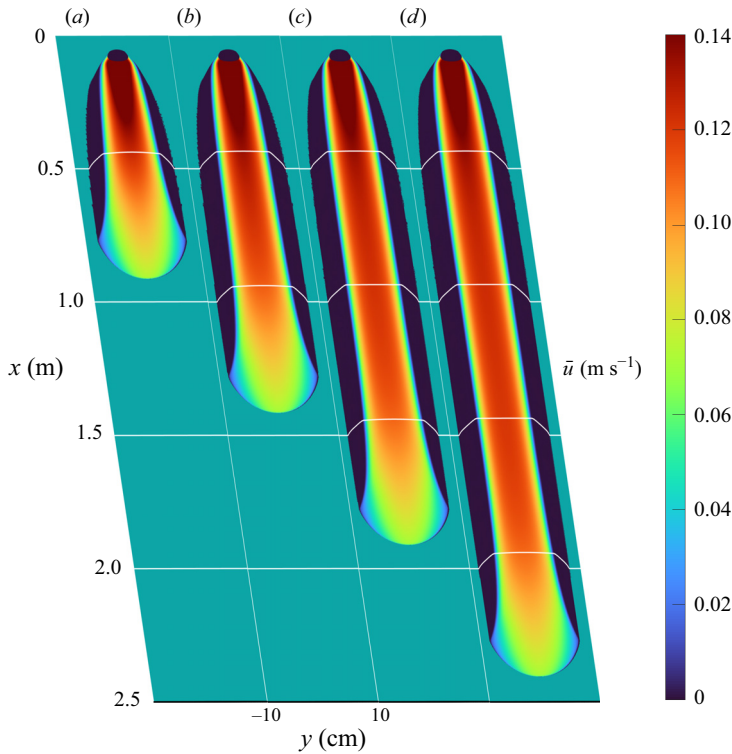
Figure 3. Surface plots of the flow thickness h for the numerical simulation of a release of particles at a flow rate of $Q_m = 130$ g s^{-1} on a plane inclined at $\zeta = 32°$, coloured by the downslope component of depth-averaged velocity $\bar{u}$ and shown at times (*a*) $t = 7$, (*b*) 14, (*c*) 21 and (*d*) 28 s. The filled black circles indicate the non-zero source region where S_{inflow} is given by (3.2) and the solid horizontal white lines indicate cross-slope flow thickness, mimicking the displacement of an experimental laser line. The online supplementary movie 1 available at https://doi.org/10.1017/jfm.2022.1089 shows the time dependent evolution of the flow.

3.2. *Depth-averaged travelling frame simulation*

For the travelling wave to be fully realised, it is useful to perform simulations in a frame moving at the front speed u_F. Using the change of coordinates

$$\tau = t - t_0, \quad \xi = x - u_F t, \tag{3.3a,b}$$

the mass and momentum conservation laws (2.2) and (2.3) can be written

$$\frac{\partial h}{\partial \tau} + \text{div}' \left(h\bar{u}' \right) = S'_{inflow}, \tag{3.4}$$

$$\frac{\partial}{\partial \tau} \left(h\bar{u}' \right) + \text{div}' \left(h\bar{u}' \otimes \bar{u}' \right) + \text{grad}' \left(\frac{1}{2} h^2 g \cos \zeta \right) = hg\boldsymbol{S} \cos \zeta + \text{div}' \left(v h^{3/2} \overline{\boldsymbol{D}'} \right), \tag{3.5}$$

where div$'$ and grad$'$ are now the two-dimensional divergence and gradient operators in the moving frame (ξ, y). The depth-averaged velocity in the moving frame is equal to $\bar{u}' = \bar{u} - u_F \boldsymbol{e}_x$. The strain-rate tensor is unchanged in the moving frame, i.e. $\overline{\boldsymbol{D}'} = \overline{\boldsymbol{D}}$. Note that the elimination of $\bar{u}$ in the transformed momentum balance (3.5) relies on subtracting u_F times the moving frame mass balance (3.4) from the transformed downslope momentum balance.

Since (3.4) and (3.5) have the same structure as the original mass and momentum balance equations (2.2) and (2.3), the numerical method described in § 3.1 can be used to compute the flow in the moving frame. This time, the computational domain is a rectangle covering the area -0.8 m $\leqslant \xi \leqslant 0.8$ m and -10 cm $\leqslant y \leqslant 10$ cm, discretized to 1600×200 finite volume cells (with the same resolution of 1 grid point per mm in both directions as the continuous release simulation). The initial conditions at $\tau = 0$ are the $t = t_0 = 28$ s state of the continuous release simulation, which is shown in figure 3(d). At the downstream boundary, at $\xi = 0.8$ m, the precursor layer enters the domain with thickness $h = h_0$ and velocity $\bar{u}' = -u_F e_x$, which is equivalent to zero velocity in the stationary frame. This condition is also trivially satisfied at the sides $y = \pm 10$ cm.

The upstream boundary condition is more complex. Physically, this is because some of the grains in the central channel are moving downslope towards the front, and therefore must enter the domain at $\xi = -0.8$ m, whilst other grains at the sides and base of the central channel, as well as in the static levees, are moving slower than the front and leave the domain. This has to be accounted for in a depth-averaged model by allowing an inflow along part of the upstream boundary and an outflow along the rest. To achieve this, a novel procedure has been developed. First, the net mass flux leaving the domain across the upstream boundary is calculated by evaluating the integral

$$Q_{out} = -\rho \int_{-W/2}^{+W/2} h\bar{u}'|_{\xi=-0.8 \text{ m}} \, \mathrm{d}y. \tag{3.6}$$

At steady state, the inflowing and outflowing grains should be in exact balance and Q_{out} should equal zero. However, the initial state is not yet quite in steady state and therefore Q_{out} is non-zero. To correct for the net loss/gain of particles across $\xi = -0.8$ m, a mass source term (similar to that applied in (3.1)) is applied across the first row of interior grid cells. The new source term in the moving frame simulations is therefore

$$S'_{inflow} = \frac{Q_{out}h|_{\xi=-0.8 \text{ m}}}{\rho \Delta x \displaystyle\int_{-W/2}^{+W/2} h|_{\xi=-0.8 \text{ m}} \, \mathrm{d}y} \tag{3.7}$$

inside the first grid cell and zero otherwise, where $\Delta x = 10^{-3}$ m is the length of a grid cell in the downslope direction. The inflow is weighted so that more mass is supplied in thicker parts of the flow. It follows that when (3.7) is integrated over the domain $(-0.8, -0.8 + \Delta x$ m$) \times (-W, W)$, it resupplies the material lost through the upstream boundary. An iterative procedure is required to refine the initial guess of $u_F = 0.07065$ m s^{-1} to ensure convergence towards a steady state. Figure 4 shows the results of a numerical simulation with $u_F = 0.07053$ m s^{-1}. Figure 4(a,b) show that the initial thickness is almost indistinguishable from the final thickness 100 s later, implying that by $t = 28$ s, the simulations in figure 3(d) were already close to steady state. The temporal evolution of Q_{out} is shown in figure 4(c). By $\tau = 100$ s, the simulation has converged on a steady state with $Q_{out} = 0$, and this is now used to reconstruct the three-dimensional velocity field near the front of a self-channelized flow with static levees.

4. Reconstruction of the three-dimensional velocity field

4.1. *Reconstruction of the bulk flow velocity components*

The depth-averaged theory in § 2 is able to quantitatively model the formation of self-channelized flows with static levees as shown by Rocha *et al.* (2019) and the
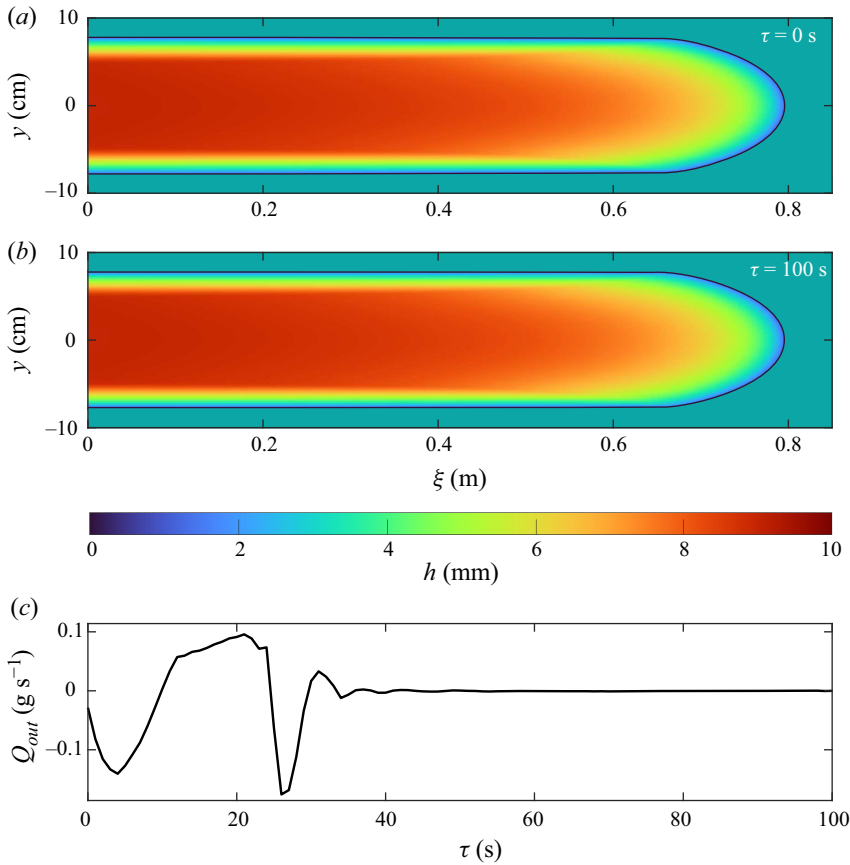
955 A38-14

Figure 4. Colour maps of flow thickness h in a frame moving with the front speed $u_F = 0.07053$ m s^{-1} plotted (*a*) at the initial time $\tau = 0$ s (equivalent to $t = t_0 = 28$ s of the continuous release simulation shown in figure 3*d*) and (*b*) after $\tau = 100$ s in the travelling frame simulation. (*c*) Mass flux Q_{out} leaving the domain as a function of time τ. This tends to zero for large times confirming that a travelling wave solution is achieved.

simulations in § 3. Following Gray & Ancey (2009) and Johnson *et al.* (2012), the three-dimensional velocity field $\boldsymbol{u} = (u, v, w)$ is reconstructed from $\bar{\boldsymbol{u}}$ by assuming a velocity profile through the depth of the flow. For a general function $f(z/h)$, the horizontal components of the three-dimensional velocity field parallel to the slope are related to their depth-averaged counterparts by

$$(u, v) = f\left(\frac{z}{h}\right)(\bar{u}, \bar{v}). \tag{4.1}$$

This paper assumes a Bagnold velocity profile (Silbert *et al.* 2001; GDR-Midi 2004; Jop *et al.* 2005; Gray & Edwards 2014; Baker *et al.* 2016*a*) which implies

$$f\left(\frac{z}{h}\right) = \frac{5}{3}\left[1 - \left(1 - \frac{z}{h}\right)^{3/2}\right]. \tag{4.2}$$

It is possible to reconstruct the three-dimensional velocity field using other profiles. For instance, Johnson *et al.* (2012) reconstructed a qualitatively similar depth-averaged velocity field $\bar{\boldsymbol{u}}$ using (i) plug flow, (ii) simple shear and (iii) linear shear with basal slip. As shown in their figure 11, this has an important affect on the surface trajectories of

particles and determines the degree to which they reach the front and are overturned, or are deposited at the surface of the static levees. For plug flow, there is no overturning, which is unrealistic, and simple shear has too much overturning compared with measurements of debris flows at the USGS flume. Johnson *et al.* (2012) found that a combination of linear shear and basal slip was the most realistic. This is also consistent with the Bagnold profile used here (Baker *et al.* 2016*b*).

Saingier, Deboeuf & Lagrée (2016) showed that when there is velocity shear, non-unity values of the velocity shape factor $\chi = \overline{u^2}/(\bar{u})^2$ in the momentum transport terms lead to the formation of a precursor layer in depth-averaged avalanche models. Since a precursor layer is not observed in experiments, they inferred that the velocity profile must become plug-like at the front, i.e. $\chi \to 1$ as $h \to 0$. Many avalanche computations therefore assume $\chi = 1$. Despite this, frontal overturning is often observed in experiments (Johnson *et al.* 2012), and also occurs in non-depth-averaged numerical simulations using the $\mu(I)$ rheology (see figures 3 and 6 of Barker *et al.* 2021). This paper therefore takes the pragmatic view. The shape factors are assumed to be unity in the depth-averaged momentum balance (2.3), but Bagnold velocity profiles are assumed everywhere, which allows the flow to overturn at the front. Support for this approach comes from Saingier *et al.* (2016) who showed that at low Froude numbers ($Fr < 1$), the Bagnold shape factor ($\chi = 5/4$) barely changes the free surface shape. Since $Fr \simeq 0.3$ in the simulations in figure 3, this is therefore a good approximation. Open questions still remain about whether the velocity profile should also be Bagnold-like in the cross-stream direction, but it is a reasonable first approximation. In addition, this paper neglects all feedback of the evolving particle-size distribution on the local velocity profile (Rognon *et al.* 2007) or the basal friction. This would require a fully coupled theory such as the depth-averaged one of Baker *et al.* (2016*b*) or the non-depth-averaged one of Barker *et al.* (2021).

Using the Bagnold profile (4.2), it follows that the horizontal components of the three-dimensional velocity field (u', v') in a frame moving with the speed of the front (3.3*a*,*b*) are

$$u' = -u_F + \frac{5}{3}(\bar{u}' + u_F)\left[1 - \left(1 - \frac{z}{h}\right)^{3/2}\right], \qquad (4.3)$$

$$v' = \frac{5}{3}\bar{v}'\left[1 - \left(1 - \frac{z}{h}\right)^{3/2}\right], \qquad (4.4)$$

respectively. Figures 5 and 6 show the three-dimensional downslope and cross-slope velocity fields reconstructed from the two-dimensional travelling wave solutions in § 3.2 at $\tau = 100$ s. In these figures, panels (*a*–*d*) show longitudinal cross-sections at equally spaced positions across the width of the flow (as indicated in panel *h*), whereas panels (*e*–*h*) show sections across the flow at regular downslope intervals (as indicated in panel *d*). The central plane (panel *a*) looks similar to a Pouliquen (1999*b*) front, with a monotonically decreasing free surface, but the downslope free-surface velocity decreases towards the front indicating that there must be lateral motion. The highest downslope velocities are attained in the thickest part of the flow in the centre of the channel, and the velocity decreases to zero towards the bottom and sides of the flow. Within the levees (panel *d* and panels *e*–*g*), the downslope velocity u is zero in the stationary frame, but in the moving frame, it appears to move upslope with velocity $u' = -u_F \simeq -0.07$ m s^{-1}. The static/slow-moving region is broadly consistent with that inferred experimentally by Deboeuf *et al.* (2006) in their figure 4, although a direct comparison with the steady state used here is not possible, due to the partial collapse of the levee walls and drainage of the channel as their flow was brought to rest. Note that Rocha *et al.* (2019) showed that

955 A38-16

the same depth-averaged model used here is able to capture this drainage and collapse (see their figures 14 and 15, and movies 5 and 6). Their model could therefore be used to reconstruct the full three-dimensional temporally evolving flow field, but that is beyond the scope of this paper.

The central flowing channel is of almost constant depth at $\xi = 0.1$ m (panel e) indicating that the flow is close to the steady-state solutions of Rocha *et al.* (2019) and becomes progressively more curved as the front is approached and the lateral motion advects the incoming grains into the slower moving parts of the flow and the static levees. The cross-slope velocity (figure 6) is antisymmetric about $y = 0$, indicating that the oncoming flow is pushed out laterally on either side of the centre plane with the highest cross-slope speeds achieved along the free surface at the sides of the spreading front. The no-net-flow line, where $u' = 0$, is shown in figure 5(e). Material that is above the no-net-flow line moves faster than the flow front ($u' > 0$) and is advected downslope, while material that is below the no-net-flow line moves slower than the front ($u' < 0$) and is transported back upstream. In the fixed laboratory frame, however, all the material is either moving downslope or is stationary.

An expression for the normal component w' of the three-dimensional velocity in the moving frame is derived by integrating the incompressibility condition (upon which the depth-averaged theory is based, see e.g. Gray & Edwards 2014; Baker *et al.* 2016a) with respect to z, subject to the condition that $w' = 0$ at $z = 0$, to give

$$w'(\xi, y, z) = - \int_0^z \left(\frac{\partial u'}{\partial \xi} + \frac{\partial v'}{\partial y} \right) d\hat{z}, \tag{4.5}$$

where $\hat{z}$ is a dummy variable. Substituting the horizontal velocity components (4.3) and (4.4) into (4.5), and using the steady-state mass balance equation in the moving frame (3.4) to simplify the result, implies that the normal velocity

$$w' = f_1 \left(\frac{z}{h} \right) u_F \frac{\partial h}{\partial \xi} - f_2 \left(\frac{z}{h} \right) h \left[\frac{\partial \bar{u}'}{\partial \xi} + \frac{\partial \bar{v}'}{\partial y} \right], \tag{4.6}$$

where the functions

$$f_1 \left(\frac{z}{h} \right) = \frac{1}{3} \left[2 - 5 \left(1 - \frac{z}{h} \right)^{3/2} + 3 \left(1 - \frac{z}{h} \right)^{5/2} \right], \tag{4.7}$$

$$f_2 \left(\frac{z}{h} \right) = \frac{5}{3} \left[\frac{z}{h} - \left(1 - \frac{z}{h} \right)^{3/2} + \left(1 - \frac{z}{h} \right)^{5/2} \right]. \tag{4.8}$$

The reconstructed normal component of velocity for the two-dimensional travelling wave solution computed in § 3.2 is illustrated in figure 7, using the same format as in figures 5 and 6. This indicates that the flow moves rapidly downwards along the free surface of the front and that there is no normal velocity in the levees. Just like u', w' is symmetric about the centreline $y = 0$.

4.2. *Reconstruction of the free-surface velocity and particle trajectories*

Figure 8(a) shows the velocity vectors in the stationary frame superimposed on top of a colour map of the downslope component of the free-surface velocity. Sufficiently far upstream, the static levees are close to their steady-state widths and there is a pronounced velocity profile across the central channel. Material is transported to the flow front along the central channel and as it nears the front, the levees decrease in width and the
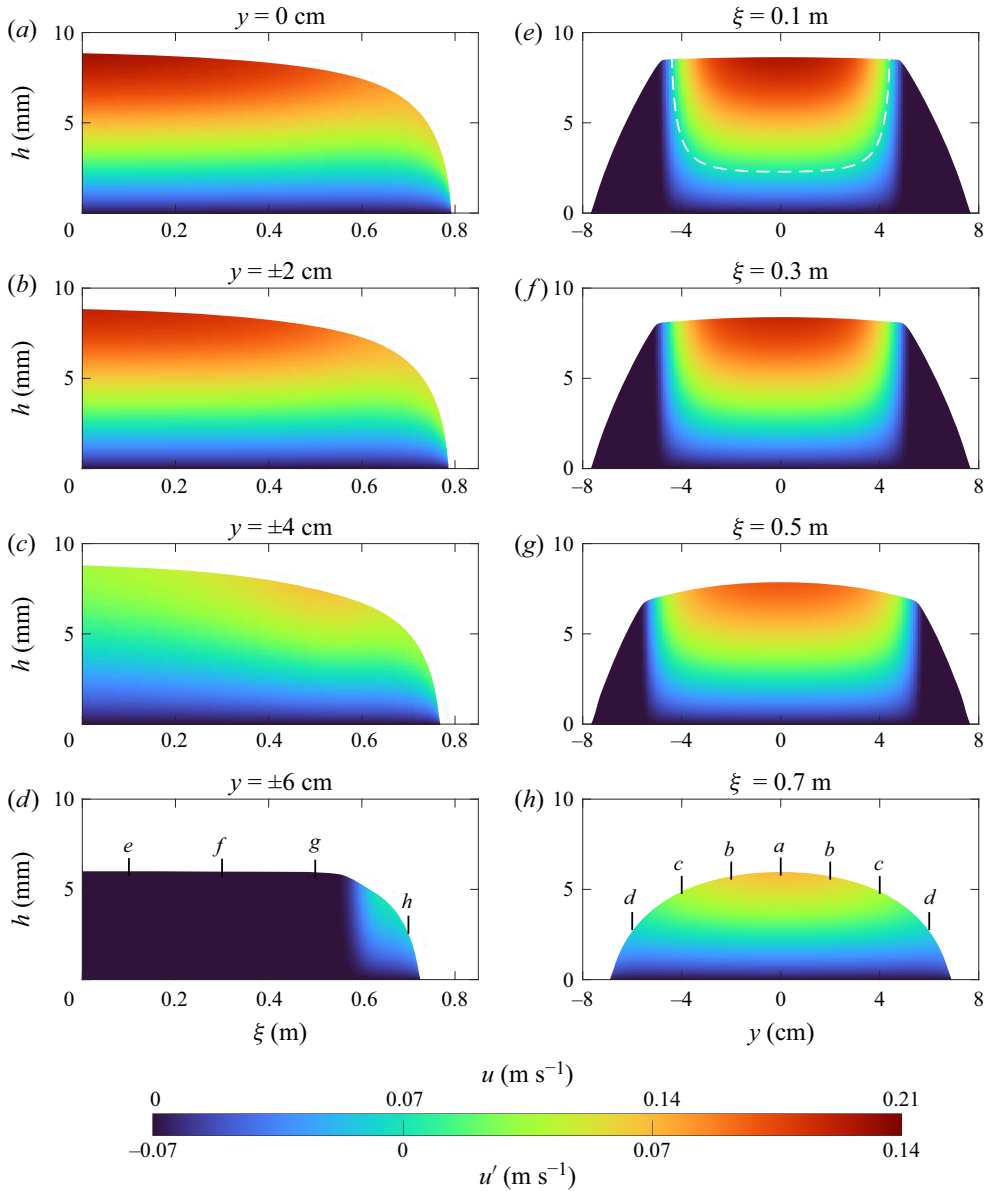
Figure 5. Colour maps of the downslope component of the three-dimensional velocity field $\boldsymbol{u}$ reconstructed from the depth-averaged travelling wave computed in § 3.2 (at $\tau = 100$ s) with front speed $u_F = 0.07$ m s^{-1}. The colour maps are shown at cross-slope positions (*a*) $y = 0$, (*b*) ± 2, (*c*) ± 4 and (*d*) ± 6 cm, and downslope positions (*e*) $\xi = 0.1$, (*f*) 0.3, (*g*) 0.5 and (*h*) 0.7 m. The relative positions of the various cross-sections are indicated by the black tick marks and corresponding labels in panels (*d,h*). A single colour scale is used to show both u and $u' = u - u_F$. The dashed white line in panel (*e*) is the no-net-flow line. It separates the region above, where the particles are moving towards the front ($u' > 0$), from the region beneath, where particles are moving away from the front ($u' < 0$). The depth-averaged flow parameters are summarized in tables 1 and 2, and a Bagnold velocity profile (4.2) is used in the reconstruction.
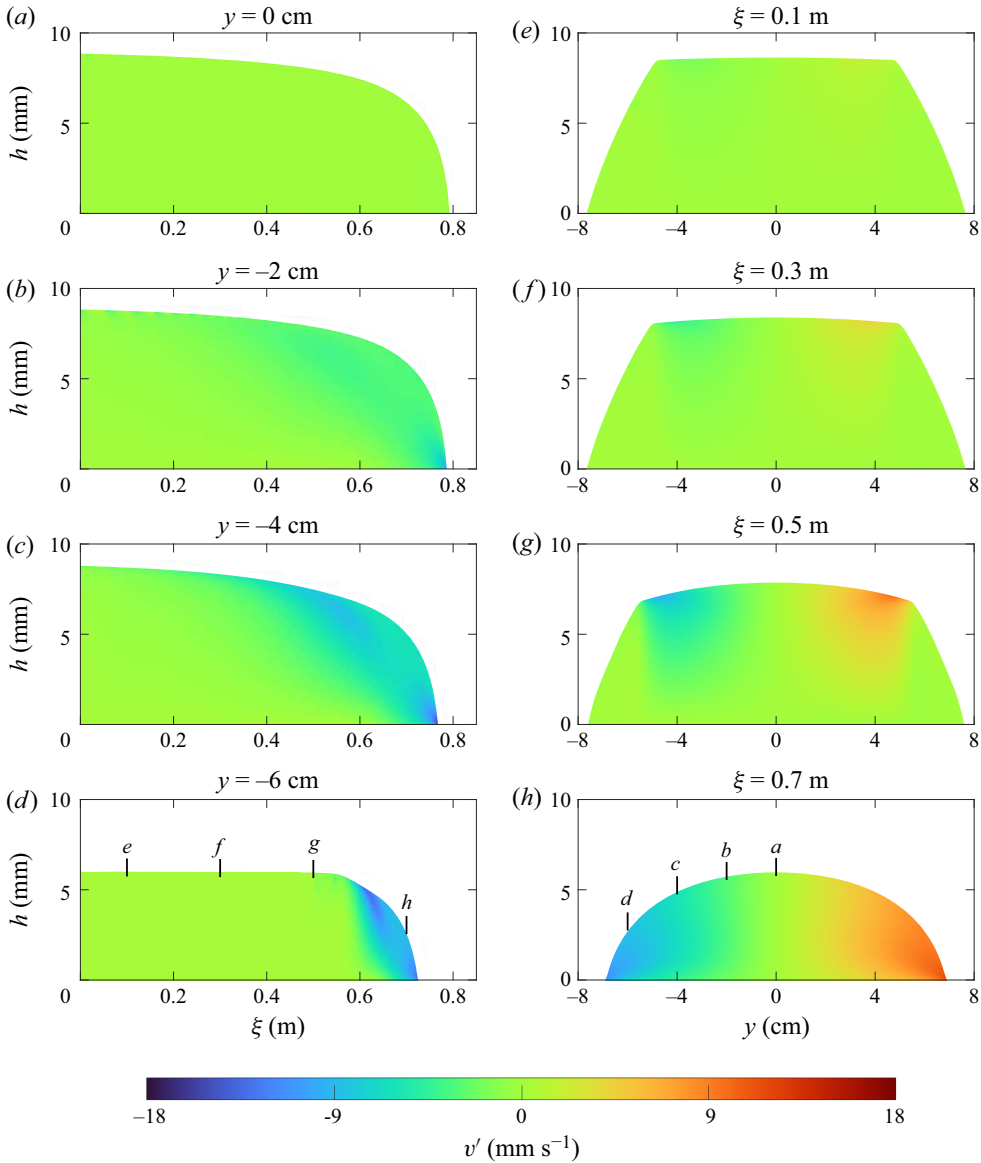
Figure 6. Colour maps of the cross-slope component $v = v'$ of the three-dimensional velocity field $\boldsymbol{u}$ reconstructed from the depth-averaged travelling wave computed in § 3.2 (at $\tau = 100$ s) with front speed $u_F = 0.07$ m s^{-1}. The colour maps are shown at cross-slope positions (*a*) $y = 0$, (*b*) -2, (*c*) -4 and (*d*) -6 cm, and downslope positions (*e*) $\xi = 0.1$, (*f*) 0.3, (*g*) 0.5 and (*h*) 0.7 m. The relative positions of the various cross-sections are indicated by the black tick marks and corresponding labels in panels (*d*) and (*h*). Note that cross-slope velocity is antisymmetric about the centre line $y = 0$. The depth-averaged flow parameters are summarized in tables 1 and 2, and a Bagnold velocity profile (4.2) is used in the reconstruction.

flow spreads out laterally and slows down. This is qualitatively similar to large-scale debris-flow experiments (see figure 9*a* of Johnson *et al.* 2012), so this relatively simple small-scale simulation captures the essential features of much larger scale geophysical flows. Figure 8(*b*) shows the same solution, but in the moving frame, so it is now
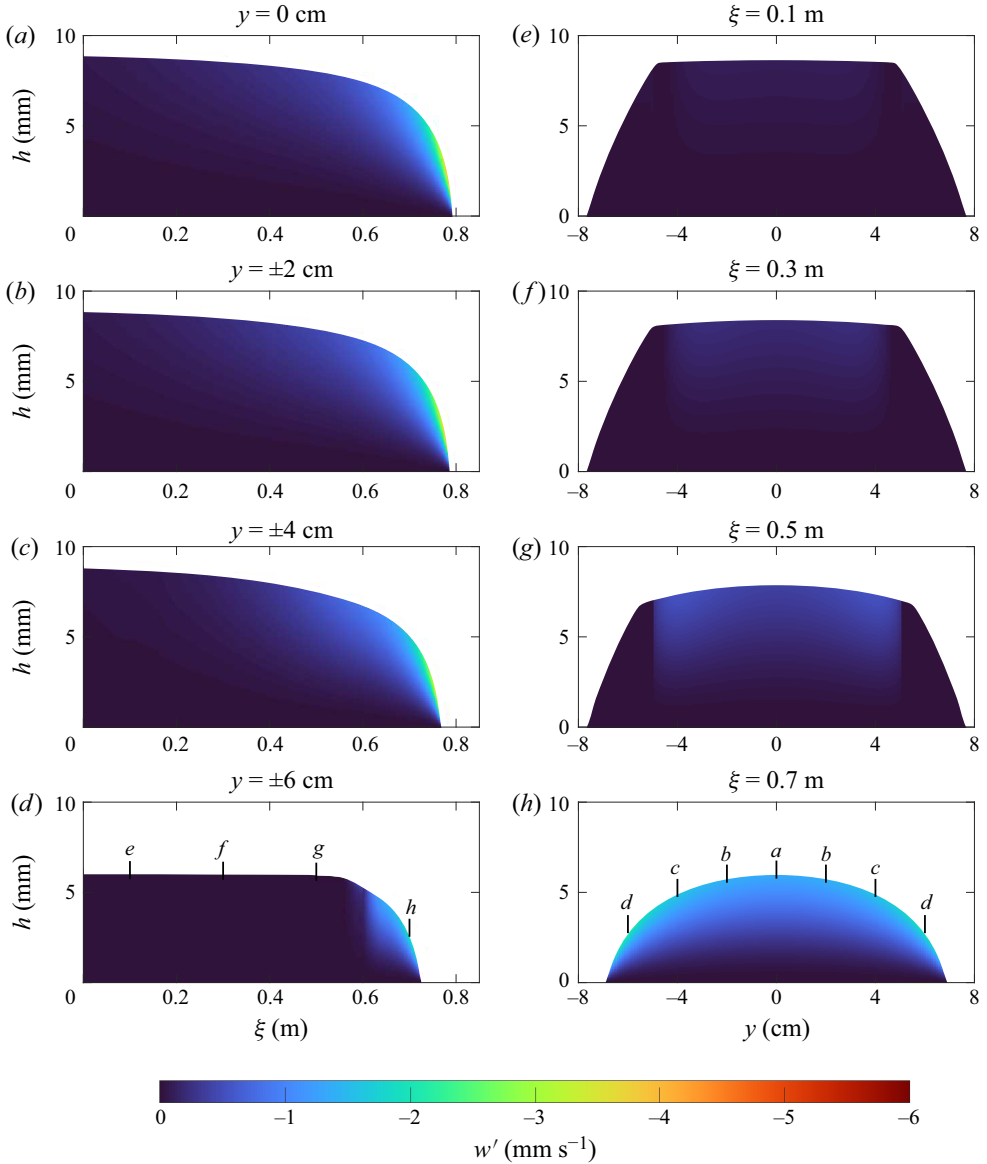
Figure 7. Colour maps of the cross-slope component $w = w'$ of the three-dimensional velocity field $\boldsymbol{u}$ reconstructed from the depth-averaged travelling wave computed in §3.2 (at $\tau = 100$ s) with front speed $u_F = 0.07$ m s^{-1}. The colour maps are shown at cross-slope positions (*a*) $y = 0$, (*b*) ± 2, (*c*) ± 4 and (*d*) ± 6 cm, and downslope positions (*e*) $\xi = 0.1$, (*f*) 0.3, (*g*) 0.5 and (*h*) 0.7 m. The relative positions of the various cross-sections are indicated by the black tick marks and corresponding labels in panels (*d*,*h*). The depth-averaged flow parameters are summarized in tables 1 and 2, and a Bagnold velocity profile (4.2) is used in the reconstruction.

possible to see that relative to the moving front, the static levees are moving backwards in accordance with the large-scale experiments in figure 9(*b*) of Johnson *et al.* (2012).

The motion of a particle at position $\boldsymbol{\xi}_p = (\xi_p, y_p, z_p)$ that is advected by the three-dimensional velocity field (u', v', w') in the moving frame of reference is determined
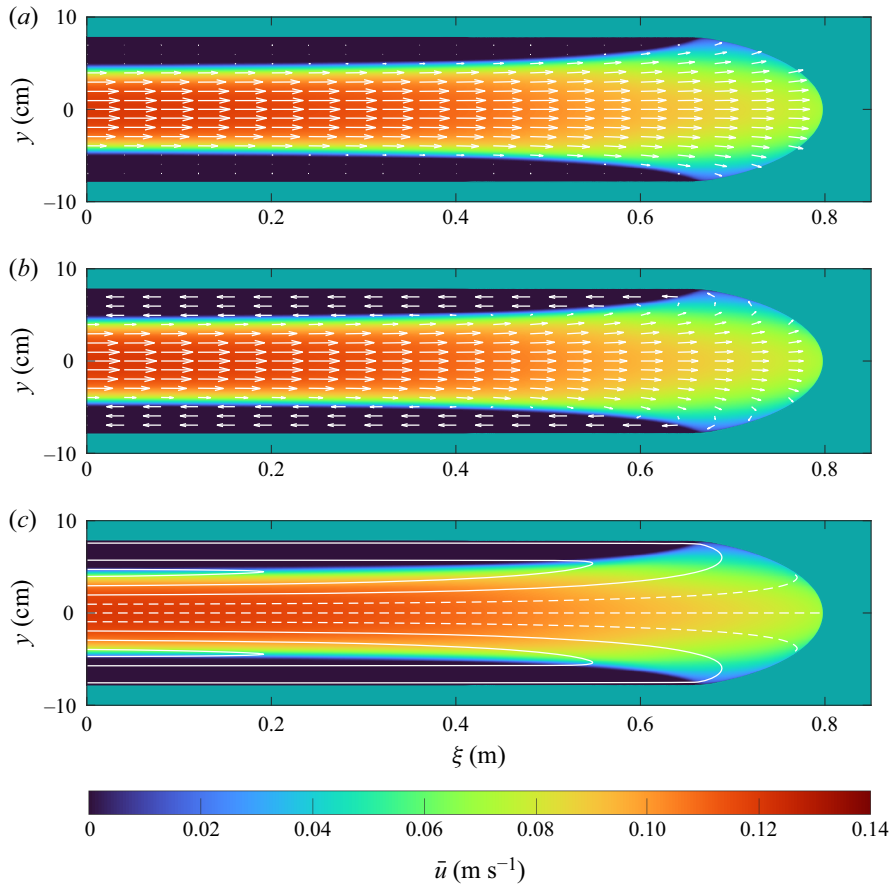
Figure 8. Plots of the surface values of (*a*) laboratory frame velocity $\boldsymbol{u}$ (white arrows), (*b*) moving frame velocity $\boldsymbol{u}'$ (white arrows), and (*c*) moving frame streamlines (solid and dashed white lines) on top of colour maps of the depth-averaged downslope velocity component $\bar{u}$. The surface velocity is shown to be greatest along $y = 0$ and the levees are stationary in the laboratory frame of reference (*a*) or equivalently propagating upslope with the front speed u_F in the moving frame (*b*). Surface material flowing down the central channel is pushed around at the lateral extents of the snout where the magnitude of the cross-slope velocity is greatest. This is depicted by the streamlines in (*c*), where the outermost trajectories in the *y*-direction turn back on themselves (solid white lines) whilst the central ones (dashed white lines) are turned over by the flow front.

by

$$\frac{\mathrm{d}\xi_p}{\mathrm{d}\tau} = u'(\boldsymbol{\xi}_p), \quad \frac{\mathrm{d}y_p}{\mathrm{d}\tau} = v'(\boldsymbol{\xi}_p), \quad \frac{\mathrm{d}z_p}{\mathrm{d}\tau} = w'(\boldsymbol{\xi}_p). \tag{4.9a–c}$$

These three-dimensional particle paths coincide with the streamlines of the bulk flow field. Figure 8(*c*) shows the reconstructed free-surface particle trajectories for the travelling wave solution in § 3.2. Particles in the centre of the channel are transported to the flow front and disappear from view as the flow overturns. Particles in the central channel that start closer to the static levees are advected downslope and are either recirculated back into the more slowly moving boundary layer adjacent to the levees, or deposited at the surface of the static levees and then move backwards away from the moving front. Again, this is exactly the behaviour that was observed in Johnson *et al.*'s (2012) large-scale debris-flow experiments (see their figures 6 and 8). This underlines the fact that the

travelling wave solution in § 3.2 and the reconstructed velocity field produces a bulk flow that is qualitatively very similar to self-channelized geophysical flows.

5. Particle-size segregation equations

In §§ 3 and 4, the thickness h and the three-dimensional velocity field $\boldsymbol{u}$ have been computed near the front of a steadily propagating monodisperse self-channelized flow. In reality, debris flows, dense pyroclastic flows and rock avalanches are composed of a wide variety of grain sizes that may segregate during motion and feedback on the bulk motion (Costa & Williams 1984; Pierson 1986; Iverson 1997; Iverson & Vallance 2001; Félix & Thomas 2004; Johnson *et al.* 2012; Kokelaar *et al.* 2014; Baker *et al.* 2016*b*; Kokelaar *et al.* 2017; Denissen *et al.* 2019; Barker *et al.* 2021). This paper focusses on how a simple bidisperse mixture is advected, segregated and deposited in a generic self-channelizing flow, without feedback effects.

5.1. *The bidisperse segregation equation*

The flow is assumed to be composed of a bidisperse mixture of large and small particles that occupy volume fractions ϕ^l and ϕ^s per unit granular volume, respectively. The volume fractions (or concentrations) necessarily sum to unity

$$\phi^s + \phi^l = 1. \tag{5.1}$$

During shear, the large grains tend to rise above smaller grains. The segregation is governed by the segregation–advection–diffusion equation for the concentration of small particles (Gray & Thornton 2005; Gray & Chugunov 2006; Gray 2018)

$$\frac{\partial \phi^s}{\partial t} + \nabla \cdot \left(\phi^s \boldsymbol{u} \right) + \nabla \cdot \left(f_{sl} \phi^s \phi^l \frac{\boldsymbol{g}}{|\boldsymbol{g}|} \right) = \nabla \cdot \left(\mathcal{D}_{sl} \nabla \phi^s \right), \tag{5.2}$$

where ∇ is the three-dimensional gradient operator, f_{sl} is the segregation-velocity magnitude, $\mathcal{D}_{sl}$ is the diffusivity of the small and large particles, and $\boldsymbol{g} = g \sin \zeta \, \boldsymbol{e}_x - g \cos \zeta \, \boldsymbol{e}_z$ is the gravitational acceleration vector expressed in slope aligned coordinates. Equation (5.2) implies that the rate of change of the small particle concentration is balanced by an advective flux due to the bulk flow, a segregation flux that shuts off when a pure region of large or small particles is formed (i.e. when $\phi^s = 0$ or 1) and a diffusive flux that smooths out the sharp concentration shocks that can otherwise form.

5.2. *Expressions for the diffusivity and the segregation-velocity magnitude*

There has been considerable recent progress in determining the functional form of f_{sl} and $\mathcal{D}_{sl}$. For monodisperse flows of disks, Utter & Behringer (2004) showed that the self diffusivity of the particles is of the form $\mathcal{D} = \mathcal{A} \dot{\gamma} d^2$, where $\mathcal{A}$ is a non-dimensional constant of proportionality, d is the grain diameter and the shear rate

$$\dot{\gamma} = \sqrt{\tfrac{1}{2} \text{tr}(\boldsymbol{D}^2)}, \quad \text{where } \boldsymbol{D} = \tfrac{1}{2} \left(\nabla \boldsymbol{u} + (\nabla \boldsymbol{u})^{\text{T}} \right), \tag{5.3}$$

is the strain-rate tensor. Trewhela *et al.* (2021) generalized this to bidisperse flows by replacing d by the volume fraction weighted local mean grain diameter

$$\bar{d} = \phi^l d^l + \phi^s d^s, \tag{5.4}$$

$\mathcal{A}$	$\mathcal{B}$	$\mathcal{C}$	Φ	R	d^l	d^s
0.108	0.7125	0.2712	0.5	1.49	0.61 mm	0.41 mm

Table 3. The universal constants $\mathcal{A}$, $\mathcal{B}$ and $\mathcal{C}$ in the diffusivity (5.5) and the segregation-velocity magnitude (5.9) measured by Utter & Behringer (2004) and Trewhela *et al.* (2021), as well as the parameter values used in § 6. Note that for the simulations presented in this paper, $\mathcal{D}_{sl}$ is assumed to be zero.

where d^l and d^s are the diameters of the large and small particles, respectively. It follows that the bidisperse diffusivity

$$\mathcal{D}_{sl} = \mathcal{A}\dot{\gamma}\bar{d}^2. \tag{5.5}$$

Refractive index matched shear box experiments (Trewhela *et al.* 2021) have also been used to show that for grain-size ratios

$$R = d^l/d^s \tag{5.6}$$

close to unity, the segregation-velocity magnitude f_{sl} scales as

$$f_{sl} = \frac{\mathcal{B}\rho_* g \dot{\gamma}\bar{d}^2(R-1)}{\mathcal{C}\rho_* g \bar{d} + p}, \tag{5.7}$$

where $\mathcal{B}$ and $\mathcal{C}$ are non-dimensional empirical constants, ρ_* is the intrinsic density of the grains and p is the pressure. In the theories of Gray & Edwards (2014) and Baker *et al.* (2016*a*), which underly the depth-averaged model used to calculate the bulk flow field in §§ 2 and 3, the pressure is lithostatic, i.e.

$$p = \rho_* \Phi g (h-z) \cos \zeta, \tag{5.8}$$

where Φ is the constant solids volume fraction (GDR-Midi 2004). Substituting (5.8) into (5.7) implies that the segregation-velocity magnitude,

$$f_{sl} = \frac{\mathcal{B}\dot{\gamma}\bar{d}^2(R-1)}{\mathcal{C}\bar{d} + \Phi(h-z)\cos\zeta}, \tag{5.9}$$

is independent of the intrinsic particle density ρ_* and the constant of gravitational acceleration g. Equation (5.9) also implies that f_{sl} is linearly dependent on the shear rate $\dot{\gamma}$ and is approximately inversely proportional to the local particle depth $h - z$. All other conditions being equal, particles at the base of the flow will therefore segregate slower than particles near the free surface. The non-dimensional constant $\mathcal{C}$ was included by Trewhela *et al.* (2021) to prevent the segregation-velocity magnitude from having a singularity at $z = h$. The values of the universal non-dimensional constants $\mathcal{A}$, $\mathcal{B}$ and $\mathcal{C}$ determined by Utter & Behringer (2004) and Trewhela *et al.* (2021) are summarized in table 3. For moderate particle-size ratios ($2 < R < 4$) and low small particle concentrations, Trewhela *et al.* (2021) observed individual small particle intruders could percolate more rapidly through a shearing matrix of large grains than suggested by (5.9). This enhanced segregation rate was related to the transition to spontaneous percolation at large size ratios. Such effects are neglected in this paper, as are enhanced packing effects at large size ratios, which can reduce the segregation rate as mixtures of grains pack more densely together.

5.3. *Scale dependence of the segregation equation*

It is also possible to show that the segregation equation (5.2) in conjunction with the diffusivity (5.5) and the segregation-velocity magnitude (5.9) are dependent on the typical particle diameter d. Introducing the general set of scalings

$$(x, y, z, h, \bar{d}, d^l, d^s) = d\,(\tilde{x}, \tilde{y}, \tilde{z}, \tilde{h}, \tilde{\bar{d}}, \tilde{d}^l, \tilde{d}^s), \quad t = (d/U)\,\tilde{t}, \quad \boldsymbol{g} = g\,\tilde{\boldsymbol{g}}, \\ (\boldsymbol{u}, f_{sl}) = U(\tilde{\boldsymbol{u}}, \tilde{f}_{sl}), \quad \dot{\gamma} = (U/d)\,\tilde{\dot{\gamma}}, \quad \mathcal{D}_{sl} = (Ud)\,\tilde{\mathcal{D}}_{sl}, \tag{5.10a–f}$$

where U is a typical velocity magnitude, it follows that the non-dimensional segregation equation

$$\frac{\partial \phi^s}{\partial \tilde{t}} + \tilde{\boldsymbol{\nabla}} \cdot \left(\phi^s \tilde{\boldsymbol{u}}\right) + \tilde{\boldsymbol{\nabla}} \cdot \left(\tilde{f}_{sl}\phi^s \phi^l \frac{\tilde{\boldsymbol{g}}}{|\tilde{\boldsymbol{g}}|}\right) = \tilde{\boldsymbol{\nabla}} \cdot \left(\tilde{\mathcal{D}}_{sl}\tilde{\boldsymbol{\nabla}}\phi^s\right), \tag{5.11}$$

the non-dimensional diffusivity

$$\tilde{\mathcal{D}}_{sl} = \mathcal{A}\tilde{\dot{\gamma}}\tilde{\bar{d}}^2 \tag{5.12}$$

and the non-dimensional segregation velocity

$$\tilde{f}_{sl} = \frac{\mathcal{B}\tilde{\dot{\gamma}}\tilde{\bar{d}}^2(R-1)}{\mathcal{C}\tilde{\bar{d}} + \Phi\,(\tilde{h} - \tilde{z})\cos\zeta} \tag{5.13}$$

are independent of any new non-dimensional groups. The non-dimensional segregation equation (5.11) is therefore scale invariant, and the typical particle diameter d completely scales out of the problem. When $U = \sqrt{gd}$, the scalings (5.10a–f) are consistent with those for the bulk dry flow (2.15a–e) and the whole system scales with the typical particle diameter d and gravity g. It is this fact that explains why the self-channelized fingered deposits in the Bessel crater in Mare Serenitatis (Kokelaar *et al.* 2017) show very similar segregation to that observed in the small-scale experiments of Pouliquen *et al.* (1997), Woodhouse *et al.* (2012) and Baker *et al.* (2016b), but with particles that have a much larger average grain diameter in a reduced gravity. Importantly, the typical particle size d scales out of the equations even when U does not scale as $\sqrt{gd}$. This implies that the solutions in §§ 6 and 7 are of direct relevance to general self-channelized flows that may have more complex scalings, e.g. the USGS debris-flow flume experiments (Johnson *et al.* 2012) where the interstitial fluid may significantly influence the rheology (Iverson 1997; Denlinger & Iverson 2001; Iverson & Vallance 2001; George & Iverson 2014).

5.4. *Reduced segregation equation in the moving frame*

Considerable insights into the effects of segregation have been obtained by constructing solutions to (5.2) in the absence of diffusion, which has the advantage that it allows the large and small particle paths to be tracked explicitly (Gray & Thornton 2005; Thornton, Gray & Hogg 2006; Thornton & Gray 2008; Gray & Ancey 2009). In this paper, it is therefore assumed that the diffusivity

$$\mathcal{D}_{sl} = 0. \tag{5.14}$$

In addition, the flow computed in §§ 3 and 4 is shallow, i.e. the typical length of the flow L is much larger than a typical flow depth H. This can be exploited to simplify the segregation term. If typical downslope and cross-slope velocities are of order U, then

955 A38-24

incompressibility implies that slope normal velocities are of order εU, where $\varepsilon = H/L$ is a small parameter. Introducing the scalings

$$(x, y, z) = L(\hat{x}, \hat{y}, \varepsilon \hat{z}), \quad (u, v, w, f_{sl}) = U(\hat{u}, \hat{v}, \varepsilon \hat{w}, \varepsilon \hat{f}_{sl}), \quad t = (L/U)\hat{t}, \quad (5.15a\text{–}c)$$

where the segregation-velocity magnitude f_{sl} is also assumed to scale as εU, the non-dimensional segregation equation (5.2) becomes

$$\frac{\partial \phi^s}{\partial \hat{t}} + \frac{\partial}{\partial \hat{x}} \left(\phi^s (\hat{u} + \varepsilon \hat{f}_{sl} \phi^l \sin \zeta) \right) + \frac{\partial}{\partial \hat{y}} \left(\phi^s \hat{v} \right) + \frac{\partial}{\partial \hat{z}} \left(\phi^s (\hat{w} - \hat{f}_{sl} \phi^l \cos \zeta) \right) = 0. \quad (5.16)$$

This shows that the downslope component of segregation (the $\sin \zeta$ term) is small compared with all the other terms and can therefore be neglected. Returning to dimensional variables and using the change of coordinates (3.3a,b), it follows that the reduced segregation equation in the moving frame is

$$\frac{\partial \phi^s}{\partial \tau} + \frac{\partial}{\partial \xi} \left(\phi^s u' \right) + \frac{\partial}{\partial y} \left(\phi^s v' \right) + \frac{\partial}{\partial z} \left(\phi^s \left(w' - f_{sl} \phi^l \cos \zeta \right) \right) = 0, \quad (5.17)$$

where the physical domain $z = h(\xi, y)$ and the velocity field $\boldsymbol{u}'(\xi, y, z)$ of the travelling wave (computed in §3 and reconstructed in §4) are now steady in the moving coordinates (ξ, y, z).

6. Particle-size segregation in a self-channelized flow

6.1. *Numerical method*

The numerical solution of the advection-segregation equation (5.17) is obtained using the method of Kurganov & Tadmor (2000), extended straightforwardly to three dimensions in the domain $-0.4 \text{ m} \leqslant \xi \leqslant 0.8 \text{ m} \times -10 \text{ cm} \leqslant y \leqslant 10 \text{ cm} \times 0 \leqslant z \leqslant 10 \text{ mm}$. The flow thickness $h(\xi, y)$ and the velocity field $\boldsymbol{u}'(\xi, y, z)$ are assumed to be steady in time and given by the depth-averaged self-channelized flow simulations in §3 and the reconstruction procedure in §4. To accurately resolve steady solutions to (5.17), the numerical discretization must be well-balanced, in the sense that the constant solutions of the segregation equation $\phi^s = 0$ and $\phi^s = 1$ are preserved exactly. Well-balanced discretizations often involve a balancing of discretized numerical fluxes with source terms to preserve exact solutions. Here there are no source terms, but instead, the numerically discretized form of the advection velocity field $\boldsymbol{u}'$ is required to be exactly divergence free and satisfy an appropriate discretization of $\boldsymbol{u}' \cdot \boldsymbol{n} = 0$ on $z = 0$ and $z = h(\xi, y)$, so that no numerical flux enters or leaves the domain over these surfaces. This procedure is described in Appendix A.

6.2. *Initial and boundary conditions*

Initially, the flow is assumed to be entirely composed of small particles, i.e. $\phi_0^s(\xi, y, z, 0) = 1.0$ everywhere, and a mixture of large and small grains are fed into the domain across the upstream boundary at $\xi = -0.4$ m. There is no flux of large or small grains across $z = 0$ and $z = h(\xi, y)$. By construction, $\boldsymbol{u}' \cdot \boldsymbol{n} = 0$ on $z = 0, h(\xi, y)$, so this boundary condition reduces to the requirement that the small particle segregation flux normal to the boundary equals zero

$$\boldsymbol{F}^s \cdot \boldsymbol{n} = -f_{sl} \phi^s \phi^l \cos \zeta \, \boldsymbol{e}_z \cdot \boldsymbol{n} = 0, \quad \text{at } z = 0, h(\xi, y). \quad (6.1)$$

The upstream boundary condition along $\xi = -0.4$ m is more complicated, because, in the moving frame, large and small grains flow in and out of the domain dependent on
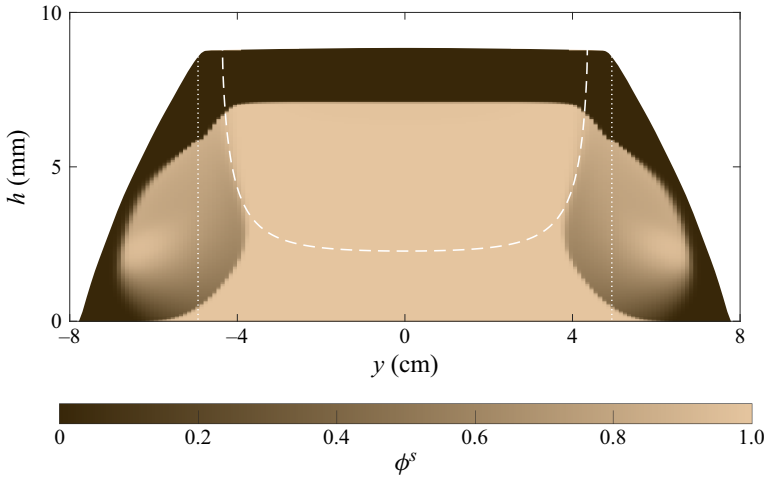
Figure 9. Colour map of the small particle concentration ϕ^s plotted at $\xi = -0.3$ m and $\tau = 100$ s for an inflow concentration $\bar{\phi}^s_{in} = 0.8$ and $R = 1.49$ with $d^l = 0.61$ mm and $d^s = 0.41$ mm. The dashed white line is the no-net-flow line, where $u' = 0$, or equivalently $u = u_F$. Above the no-net-flow line, the concentration is prescribed at the inflow at $\xi = -0.4$ m, with the large particles being sharply segregated from the small particles beneath. All the grains entering above the no-net-flow line are advected towards the flow front, segregate and eventually flow out of the domain below the no-net-flow line. The concentration below the no-net-flow line is determined by the downstream problem, and no boundary conditions are required. The white dotted lines indicate the levee-channel boundary.

whether they lie above or below the no-net-flow line. The no-net-flow line is illustrated in figure 9. The inflowing grains are assumed to be inversely graded, with the large grains separated from the small grains beneath by a sharp interface $\eta(y)$. This is assumed to be a multiple of the inflow thickness

$$\eta(y) = \bar{\phi}^s_{in} h(-0.4, y), \qquad (6.2)$$

where $\bar{\phi}^s_{in}$ is a constant. Since the inflow thickness is almost constant across the flowing part of the channel, the interface height η is almost constant, as illustrated in figure 9. The small particle concentration for the inflowing particles (above the no-net-flow line) is therefore

$$\phi^s(-0.4, y, z, t) = \begin{cases} 0, & z > \eta(y), \\ 1, & z \leqslant \eta(y). \end{cases} \qquad (6.3)$$

For the out-flowing grains that lie below the no-net-flow line in figure 9, no boundary condition is required, and the concentration that develops within the domain is simply advected upstream out of the domain.

Note that in figure 9, the large and small particles in the levees are not subject to further segregation because the shear rate $\dot{\gamma} = 0$. Segregation does, however, continue in the mixed regions that lie in the central channel. The segregation rate is small, vanishingly so right at the margins, so it takes a very long time for the large particles to fully segregate. As a result of this and the finite domain size, some large particles flow out of the domain in an unstably stratified configuration. For example, all the mixed material in the central channel has further to segregate in figure 9. The steady-state results presented here are therefore dependent on the domain size, but only weakly so, since most of the large particles in the mixed regions would ultimately segregate to positions that lie below the no-net-flow line, so they do not affect the inflow. In reality, debris flows are only sustained in quasi-steady

955 A38-26

configurations for finite periods of time, so applying the upstream boundary condition at a finite distance from the front is more realistic than considering a semi-infinite avalanche.

Provided that the inflow is sufficiently far back, the outflowing grains on the centreline of the channel are small. It follows that $\bar{\phi}_{in}^s$ is actually the depth-averaged small particle concentration in the centre of the channel. The parameter $\bar{\phi}_{in}^s$ will therefore be used to describe the mixture composition. Note that $\bar{\phi}_{in}^s$ is not equal to the composition of the arrested mixture, because the large particles near the free surface are moving faster than the small particles beneath, and a thin layer of large particles may therefore produce a larger flux than a thicker layer of small grains (Gray & Ancey 2009; Wiederseiner *et al.* 2011).

For the simulations in this section,

$$\bar{\phi}_{in}^s = 0.8, \quad \bar{\phi}_{in}^l = 1 - \bar{\phi}_{in}^s = 0.2. \quad (6.4a,b)$$

The volume fraction weighted mean particle diameter of the inflowing mixture,

$$\bar{d}_{in} = \bar{\phi}_{in}^l d^l + \bar{\phi}_{in}^s d^s, \quad (6.5)$$

is chosen to equal the particle diameter $d = 0.45$ mm (table 1) used to compute the bulk flow field in § 3. The diameters of the large and small grains, d^l and d^s, are still free to be chosen, allowing flows with different grain-size ratios R to be investigated, whilst preserving $\bar{d}_{in} = 0.45$ mm. For the simulations in this section, $d^l = 0.61$ mm and $d^s = 0.41$ mm, giving a grain-size ratio $R = 1.49$.

6.3. *Concentration profiles*

The three-dimensional small-particle concentration $\phi^s(\xi, y, z, \tau)$ is computed as a function of time τ, subject to the initial and boundary conditions described in § 6.2. The temporal evolution of the depth-averaged small-particle concentration

$$\bar{\phi}^s(\xi, y, \tau) = \frac{1}{h} \int_0^h \phi^s(\xi, y, z, \tau) \, dz, \quad (6.6)$$

towards a steady-state solution is shown in figure 10. Vertical downslope and cross-slope sections across the steady-state are shown in figure 11. Movie 2 shows the simultaneous temporal evolution of the small-particle concentration $\phi^s(\xi, y, z, \tau)$ in each of the cross-sections, as well as the depth-averaged small-particle concentration $\bar{\phi}^s(\xi, y, \tau)$. The large and small particle trajectories on the centreline are superimposed on top of the small-particle concentration distribution in figure 12. Note that although the solutions are computed for -0.4 m $< \xi$, all these plots focus on the solution near the front in the range $0 \leqslant \xi \leqslant 0.8$ m.

At early times ($\tau < 10$ s), the grains that flow into the domain at the upstream boundary (at $\xi = -0.4$ m) are already inversely graded and do not need to segregate vertically. The surface layer of large particles is therefore simply advected downstream by the bulk velocity field u', and consequently moves rapidly towards the front in the centre of the channel, spreading very little laterally, as shown in figure 10(*a*). It is only when this layer approaches the front, where the lateral velocity v' becomes significant for $\xi > 0.5$ m (figure 6), that the large particles begin to spread laterally at the surface (figure 10*b*).

At approximately $\tau = 10$ s, the leading edge of the free-surface layer of large particles reaches the front (figure 10*b*). Since the bulk flow wraps back on itself (figure 5), the large basal particles are transported backwards relative to the moving front.
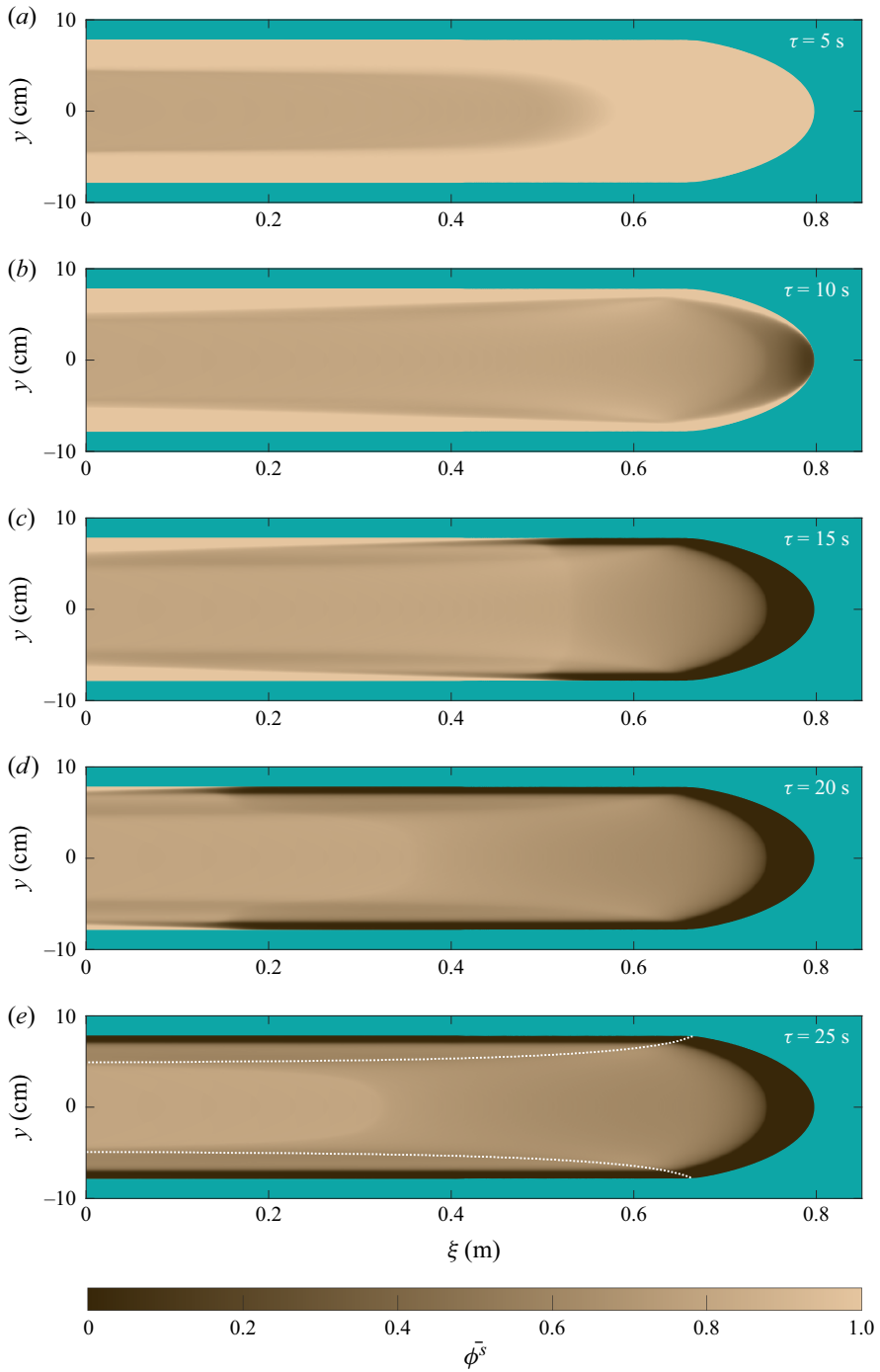
955 A38-27

Figure 10. Colour maps of depth-averaged small-particle concentration $\overline{\phi^s}$ at (*a*) $\tau = 5$, (*b*) 10, (*c*) 15, (*d*) 20 and (*e*) 25 s in the moving frame for $\bar{\phi}^s_{in} = 0.8$, $d^l = 0.61$ mm and $d^s = 0.41$ mm, which implies the grain-size ratio $R = 1.49$. The white dotted lines in panel (*e*) indicate the levee–channel boundary. The online supplementary movie 2 shows the time dependent evolution of the flow towards steady state.
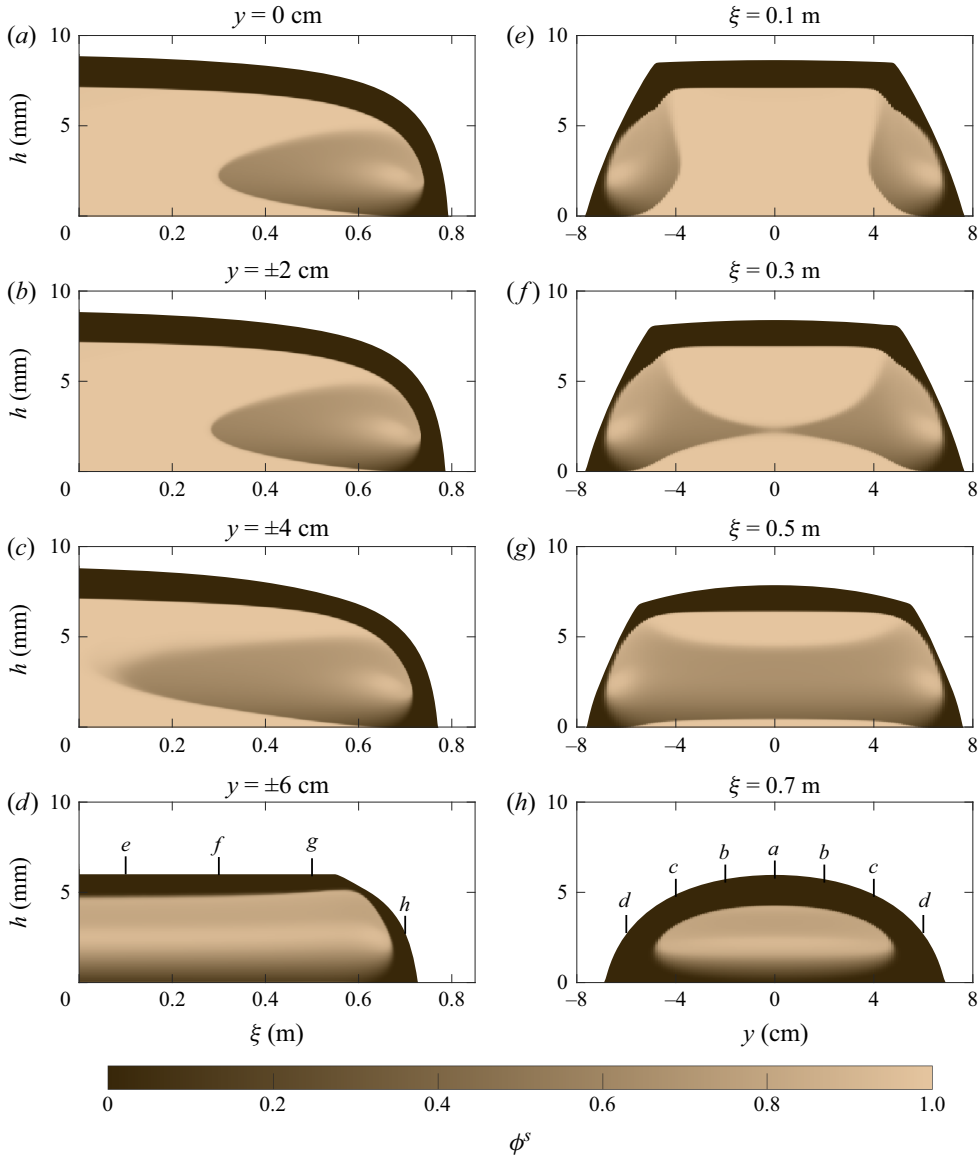
Figure 11. Colour maps of the small particle concentration ϕ^s at time $\tau = 100$ s for $\bar{\phi}^s_{in} = 0.8$, $d^l = 0.61$ mm and $d^s = 0.41$ mm ($R = 1.49$) are plotted at cross-slope positions (a) $y = 0$, (b) ± 2, (c) ± 4 and (d) ± 6 cm, and downslope positions (e) $\xi = 0.1$, (f) 0.3, (g) 0.5 and (h) 0.7 m. These locations are indicated by the black tick marks and corresponding labels in panels (d,h). The online supplementary movie 2 shows the time-dependent evolution towards the steady state in each of the sections.

Physically, this corresponds to fast moving large grains at the free surface, flowing down over the front and entering a stationary or slow moving basal region, where the downstream velocity u is much slower than the front speed u_F (figure 5). Large basal particles in the centre of the channel are therefore overrun by finer grained material, and begin to segregate upwards again (see movie 2 panels (a–c) at $\tau = 10$–35 s). In the moving frame, the segregating basal large particles initially appear to move backwards away from the front, because $u < u_F$ near the base, but they eventually reach a flow height where $u > u_F$ and
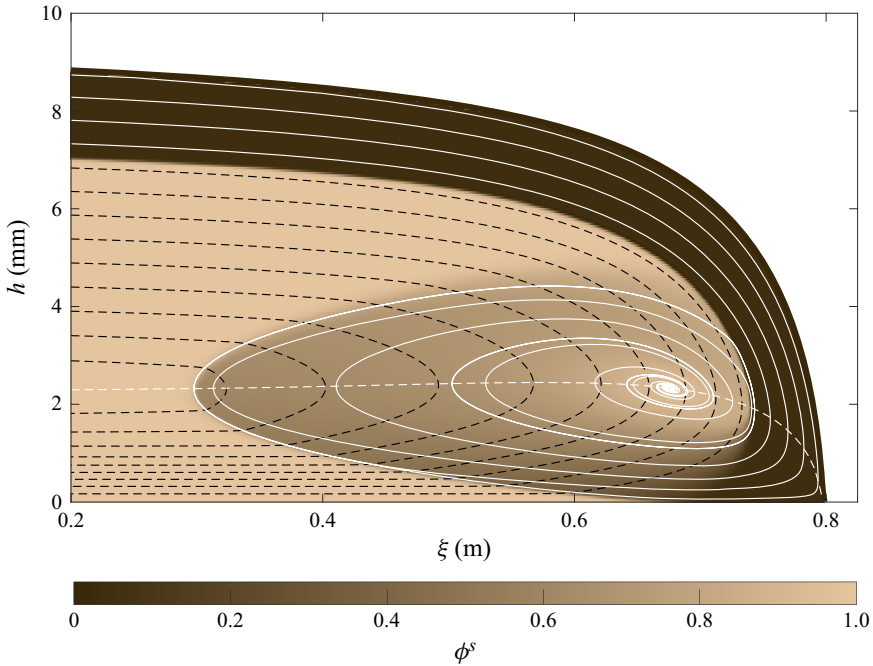
Figure 12. Steady-state small-particle concentration ϕ^s for $\bar{\phi}_{in}^s = 0.8$, $d^l = 0.61$ mm and $d^s = 0.41$ mm ($R = 1.49$) showing an enlarged view ($\xi \in [0.2, 0.8]$) of the breaking-size-segregation wave on the centreline $y = 0$. The plot also shows the large-particle paths (solid white lines), the small-particle paths (dashed black lines) and the no-net-flow line (dashed white line).

start moving forwards towards the front again. This forms a recirculating loop. This process of large particle transport, segregation and recirculation generates a diffuse small-particle concentration region that is called a breaking size-segregation wave (Thornton & Gray 2008; Gray & Ancey 2009; Gray & Kokelaar 2010; Johnson *et al.* 2012; Barker *et al.* 2021). In this three-dimensional flow, the breaking-size-segregation wave reaches a steady travelling state (figure 11) that moves downslope at the same speed as the front.

Thornton & Gray (2008) derived an exact solution for the structure of the breaking-size-segregation wave in a two-dimensional flow field. They showed it consisted of two expansion fans and two concentration shocks that were arranged in a lens-like structure that travelled downslope at a speed that was equal to the depth average of the downslope velocity over the height of the wave. Since breaking waves do not occupy the full height of the flow, this implies that in two dimensions, they move slower than the depth-averaged speed of the flow. Above them, there is a layer of large grains that moves faster than the breaking wave, and these large particles are therefore transported forwards. In two dimensions, this allows a large-rich region to form ahead of the wave, and grow in time as increasingly more large grains accumulate there (Gray & Kokelaar 2010).

Figures 10(*c–e*) and 11 show that in a fully three-dimensional flow, a large-rich snout also develops, but it travels at the same speed as the breaking-size-segregation wave just behind it. For the breaking wave to move at the same speed as the flow front, there must be a physical mechanism that removes the large particles that are transported to the flow front. In two dimensions, Gray & Ancey (2009) showed it was possible to do this by depositing the large frontal grains in a static layer at the base of the flow. In three dimensions, the

frontal large particles can instead be removed by transporting them laterally out of plane. This is what happens in the self-channelized flows studied here.

On the centreline of the channel, $v' = 0$, and the small-particle concentration equation (5.17) can be written in the form

$$\frac{\partial \phi^s}{\partial \tau} + \frac{\partial}{\partial \xi} \left(\phi^s u' \right) + \frac{\partial}{\partial z} \left(\phi^s \left(w' - f_{sl} \phi^l \cos \zeta \right) \right) = -\phi^s \frac{\partial v'}{\partial y}. \quad (6.7)$$

Since this equation is no longer dependent on cross-slope gradients of ϕ^s, the small-particle concentration $\phi^s(\xi, 0, z, \tau)$ can be solved for on the centreline provided $\boldsymbol{u'}$ is prescribed. Johnson *et al.* (2012) exploited this to compute the steady-state concentration on the centreline in a qualitatively similar flow field to that used here. This showed that the structure of the breaking-size-segregation wave was much more complicated than the two-dimensional solution of Thornton & Gray (2008).

This paper goes much further by computing the three-dimensional time-dependent structure of the breaking-size-segregation wave in a self-channelized flow field. On either side of the centreline (figure 11*b*,*c*), the concentration distribution looks qualitatively similar to that on the centreline (figure 11*a*). However, the breaking wave extends progressively further upstream (figure 11*c*) as the slower moving sides of the central channel are approached. This is due to the reduced shear rate in the channel margins, which reduces the segregation rate (5.9). As a consequence, the basal large particles take longer to segregate upwards and then be transported towards the front again, which extends the length of the breaking wave. If the large particles are incorporated into the static levees, they do not segregate further at all (figure 11*d–h*).

In the centre of the channel, the breaking size-segregation wave has a high small-particle concentration eye, which sits just behind the flow front, on the no-net-flow line. A swirl of high large-particle concentration wraps underneath and around the eye, as shown in an enlarged view in figure 12, and progressively diminishes in strength. This characteristic breaking-wave swirl is present throughout the central channel (figure 11*a–c*). At the sides of the front, the bulk flow rotates the concentration distribution in the breaking-size-segregation wave through ninety degrees and transports it laterally, partially depositing it into the static levees (figure 11*e–g*). The levees are therefore not solely composed of large particles. Instead, there is a carapace of large particles that is wrapped around the top and bottom surfaces, and a central mixed core with higher concentrations of fine grains. This is consistent with the experimental observations of Kokelaar *et al.* (2014) who used a resin impregnation technique to make sections across the levees (see their figures 5–7).

Movie 2 shows how the small-particle concentration distribution is advected from the central channel into the levees, where it is frozen in to the static deposit. In particular, as the large particles reach the front and are advected sideways and deposited into the levee walls, a large-particle-rich deposited region propagates backwards relative to the moving front in the overhead views in figure 10(*c–e*). The large-rich carapace is fully developed by $\tau = 25$ s. The steady-state development of the finer grained levee core takes considerably longer (approximately $\tau = 50$–60 s). This is because the large particles, which form this structure, have been recirculated by the breaking-size-segregation wave and take longer to get there. Movie 2 shows this as a concentration swirl that progressively develops in the levee walls. It is important to realize that this swirl is not caused by motion of the large particles in the static levees, but just by their different arrival times in the static deposit and subsequent transport away from the front in the moving frame of reference. In the final, fully developed steady state, shown in figure 11, all the large and small particles that

955 A38-31

enter above the no-net-flow line at the upstream boundary at $\xi = -0.4$ m, exit the domain below the no-net-flow line (figure 9).

6.4. *Particle trajectories*

As in § 4.2 for the bulk flow, the large and small particle paths $\boldsymbol{\xi}_p^\nu = (\xi_p^\nu, y_p^\nu, z_p^\nu)$ can be reconstructed by solving the particle-path equations

$$\frac{\mathrm{d}\xi_p^\nu}{\mathrm{d}\tau} = u^\nu(\boldsymbol{\xi}_p^\nu), \quad \frac{\mathrm{d}y_p^\nu}{\mathrm{d}\tau} = v^\nu(\boldsymbol{\xi}_p^\nu), \quad \frac{\mathrm{d}z_p^\nu}{\mathrm{d}\tau} = w^\nu(\boldsymbol{\xi}_p^\nu), \tag{6.8a–c}$$

for each particle phase $\nu = l, s$. In the absence of diffusion, the bidisperse segregation equation (5.17) implies (Gray & Ancey 2009; Johnson *et al.* 2012; Gray 2018) that in the moving frame of reference, the large and small-particle velocity components are

$$u^l = u', \quad v^l = v', \quad w^l = w' + f_{sl}\phi^s \cos\zeta, \tag{6.9a–c}$$

$$u^s = u', \quad v^s = v', \quad w^s = w' - f_{sl}\phi^l \cos\zeta, \tag{6.10a–c}$$

respectively. Equations (6.8a–c) are integrated forwards in time, from the particle's initial position $\boldsymbol{\xi}_{p0}^\nu = (-0.4, y_{p0}^\nu, z_{p0}^\nu)$, above the no-net-flow line in figure 9, through the downstream flow field, until the particle exits the domain (below the no-net-flow line) across the $\xi = -0.4$ m plane.

The centreline $y = 0$ is a somewhat pathological case, because $v' = 0$. The particle trajectories therefore stay on the centreline, even though mass is constantly being transported laterally out of plane by the velocity gradient term $\partial v'/\partial y$ on the right-hand side of (6.7). The large and small particle trajectories on the centreline are superimposed on top of the small-particle concentration distribution in a zoomed-in view ($\xi \in [0.2, 0.8]$) in figure 12. Large particles enter the flow adjacent to the free surface, and move parallel to it until they near the flow front. At the front, all the large particles are overrun, and then move backwards (in the moving frame of reference) in the slower moving flow below the no-net-flow line. As they do so, they segregate upwards into progressively faster moving parts of the flow, and when they eventually cross the no-net-flow line, they begin moving forwards towards the front again. This process of being overrun by the bulk flow, segregating upwards and recirculating forwards is repeated many times. However, unlike the two-dimensional depositing flow of Gray & Ancey (2009), the large-particle paths do not form closed recirculating loops, but instead spiral in to an eye of high small-particle concentration that is centred on the no-net-flow line.

Large particles that initially move along the free surface are transported to the bottom of the flow and take longest to recirculate forwards. The free-surface large-particle trajectories therefore delineate the back of the breaking-size-segregation wave. Small particles enter the domain above the no-net-flow line, but beneath the sharp interface with the large particles (at $z = \bar{\phi}_{in}^s h$) imposed by the inflow conditions (6.2) and (6.3). All the small particle trajectories shown in figure 12 move towards the front, pass through the breaking-size segregation wave, exit beneath the no-net-flow line and then move backwards out of the domain. It is also possible (not shown) for small particles to be recirculated further upstream by the bulk flow field alone, without ever reaching the breaking-size-segregation wave. In both cases, small particles that start in the highest fastest moving part of the flow end up at or near the base, whereas those that start just above the no-net-flow line exit the domain just beneath it. However, it should be noted that the lateral velocity gradient $\partial v'/\partial y$ term in (6.7) also continuously transports a mass of small particles laterally during the recirculation.

Figure 13(*a*) and movie 3 show selected three-dimensional particle paths for the bulk flow field, reconstructed using (4.9*a–c*). The particle paths are colour coded by their inflow position above the no-net-flow line in the $\xi = 0$ plane to help identify them. From their initial location above the no-net-flow line, the particles are initially transported towards the flow front, but are then recirculated by the bulk flow field into regions of the flow that are moving slower than the front speed, and move backwards out of the domain below the no-net-flow line. Bulk particle paths near the centre of the channel move towards the front, where they are overrun by the bulk flow, whilst particles starting closer to the sides of the central channel are advected outwards and deposited into the levees before moving out of the frontal domain.

The start and end positions of the trajectories on the $\xi = 0$ plane can be interpreted as a mapping. Figure 14(*a*) shows such a mapping using the same colour map that is used to identify the trajectories in figure 13(*a*). The colour map is defined on a regular grid that lies above the no-net-flow line. This is where the particles flow into the domain towards the front. The outgoing trajectories are shown on a deformed grid and colour map below the no-net-flow line. By comparing regions of the same colour above and below the no-net-flow line in figure 14(*a*), one can identify where inflowing material flows out of the domain. Material entering at the surface of the flow in the centre of the channel therefore flows out of the domain close to the base of the central channel, while material that starts closer to the sides of the central channel ends up in the levees. In particular, for starting positions that are sufficiently far off centre, particles starting on the surface remain at the surface and are deposited near the top of the levees.

Figure 13(*b*) and movie 4 show selected three-dimensional large-particle paths starting from their inflow position above the concentration discontinuity near the free surface. Large particles in the centre of the flow are transported forwards to the front, where they are overridden by the bulk flow and appear to move backwards. However, they are able to segregate in the breaking-size-segregation wave and move up into progressively faster moving regions of the flow. This allows them to eventually move forwards and create looping trajectories as the grains are subsequently transported laterally into the levee walls. The mapping between the inflow and outflow positions is shown in figure 14(*b*). The recirculating loops generate a swirl-like structure in the core of the levee, as shown in the mapping in figure 14(*b*). Conversely, large particles that start closer to the sides of the central channel end up on the surface of the levee to form a large-rich carapace.

Figure 13(*c*) and movie 5 show selected three-dimensional small-particle paths that start between the no-net-flow line and the concentration discontinuity. They look qualitatively very similar to those of the bulk flow field, although particle segregation speeds their descent to the base of the flow. The small particles are all recirculated internally to the flow, so that none appear on the free surface. As shown in figure 14(*c*), small particles that start closer to the sides of the central channel tend to mix with the large grains and form the swirls that are deposited in the levee cores, consistent with the experimental observations of Kokelaar *et al.* (2014). These simulations also explicitly show that a pure layer of fine particles forms at the base of the flow, and that the lateral margins of the central channel and the internal levee wall are fines rich. As Kokelaar *et al.* (2014) pointed out, this fines lining could be very significant, because in fully coupled simulations (Barker *et al.* 2021, figure 7) a basal fine-grained layer significantly enhances the flow's speed.

7. Dependence on the particle-size ratio and inflow concentration

There are many parameters in the theory that are summarized in tables 1 and 3, and it is useful to say something about the values that have been chosen. Those in table 1 are
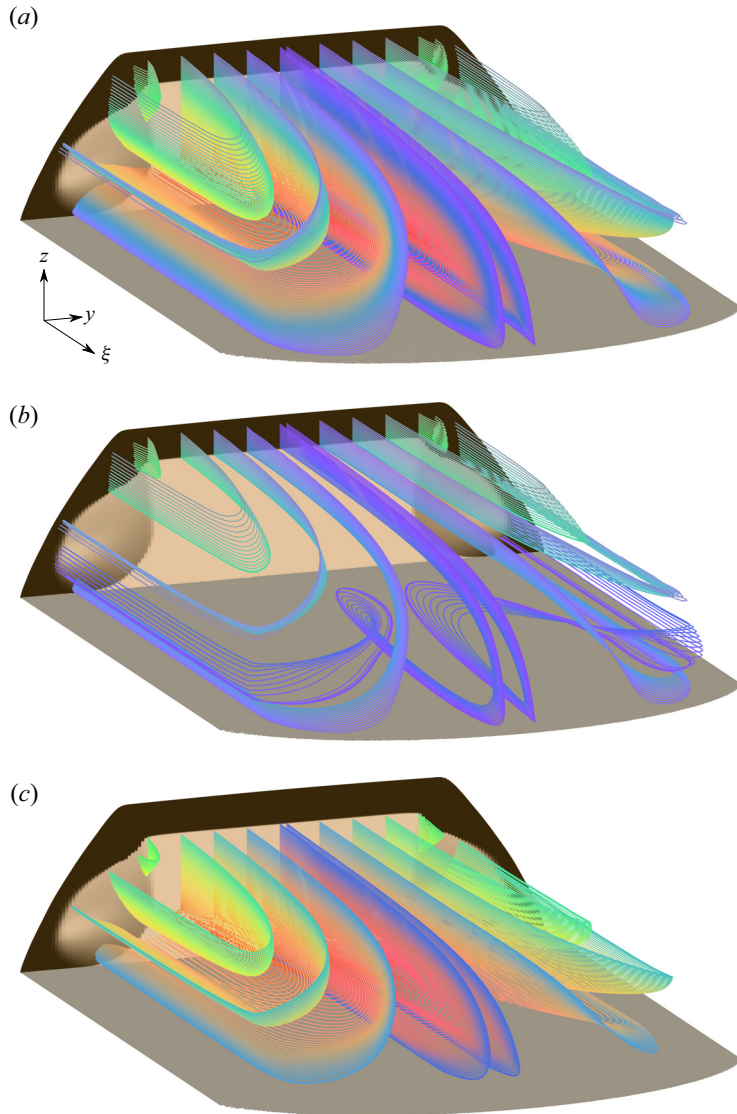
Figure 13. Three-dimensional particle trajectories starting and ending in the $\xi = 0$ plane for (*a*) the bulk flow, (*b*) large particles and (*c*) small particles. The small particle concentration ϕ^s is shown at the back of the flow in the $\xi = 0$ plane and the area of the base of the flow at $z = 0$ is filled in grey. The trajectories are coloured by their starting positions above the no-net-flow line to help identify them. These trajectory colours are used in figure 14 to show where inflowing particles starting at different locations are mapped to in the outflow. Movies 3–5 in the online supplementary material show flyby animations of the paths.

associated with the bulk flow and are tightly constrained by existing experiments and discrete element simulations (Silbert *et al.* 2001; Pouliquen & Forterre 2002; GDR-Midi 2004; Jop *et al.* 2006; Edwards *et al.* 2019; Rocha *et al.* 2019). Moreover, Takagi *et al.* (2011) performed monodisperse self-channelization experiments over a range of fluxes and showed that the flow height in the centre of the channel stayed constant, whilst the channel width increased linearly with increasing mass flux. Rocha *et al.* (2019) were able to quantitatively match these observations with the avalanche model used in this paper.
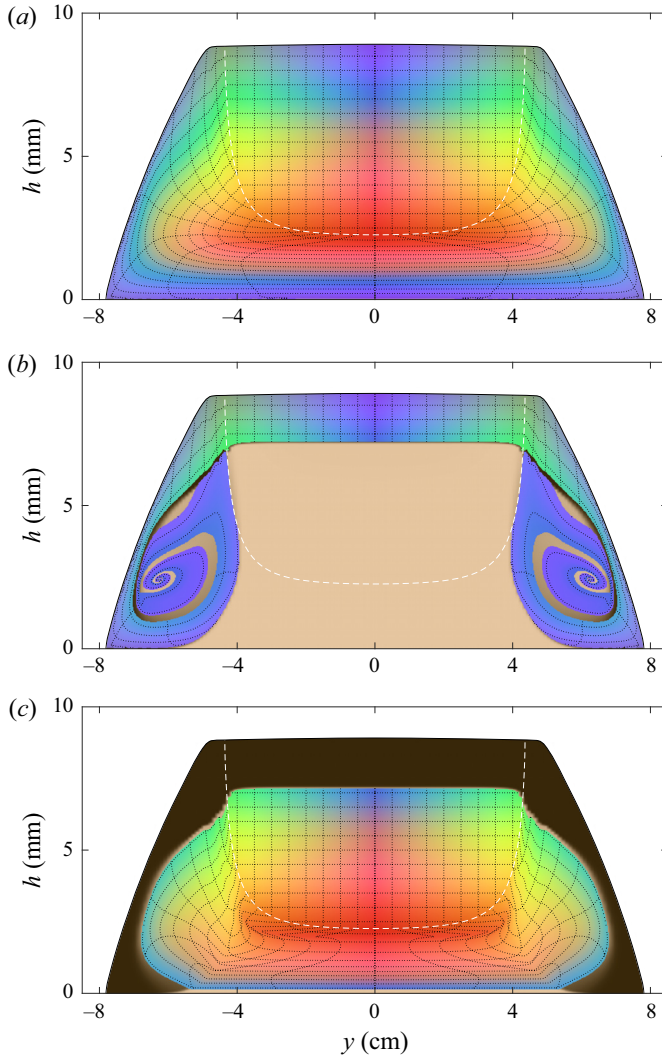
Figure 14. Mapping between the inflow and outflow positions on the $\xi = 0$ plane of the three-dimensional particles trajectories shown in figure 13 for (*a*) the bulk flow field, (*b*) large particles and (*c*) small particles. The colour scheme is the same as that used to identify the trajectories in figure 13. The initial positions of the particles are shown with a colour map and regular grid above the no-net-flow line (dashed white line). The corresponding outgoing positions are shown with the deformed grid and colour map. The steady-state concentration $\phi^s(0, y, z)$ is shown in the background.

The qualitative features of the flow field are therefore already understood in detail from the work of Rocha *et al.* (2019), and a representative case has been chosen here to look at its effects on the resultant segregation.

The non-dimensional parameters $\mathcal{A}$, $\mathcal{B}$, $\mathcal{C}$ (table 3) are universal constants that are associated with the diffusivity (5.5) and the segregation velocity magnitude (5.9) and do not need to be varied (Utter & Behringer 2004; Trewhela *et al.* 2021). The most important parameters in the system are the input conditions, i.e. the mass flux, the particle sizes and the mixing ratio. However, §§ 2.4 and 5.3 have shown that both the bulk flow and the segregation scale with the particle size. Large-scale flows of boulders and rock fragments

Panels	$R = d^l/d^s$	d^l	d^s
(a,e)	1.63	0.65 mm	0.40 mm
(b,f)	1.49	0.61 mm	0.41 mm
(c,g)	1.36	0.57 mm	0.42 mm
(d,h)	1.23	0.53 mm	0.43 mm

Table 4. The particle diameters corresponding to the assumed particle-size ratio in each panel of figure 15. The particle diameters are chosen so that when $\bar{\phi}_{in}^s = 0.8$, the average particle diameter at the inflow $\bar{d}_{in} = \bar{\phi}_{in}^l d^l + \bar{\phi}_{in}^s d^s = 0.45$ mm.

may therefore be directly equivalent to small-scale bidisperse flows with millimetre-sized grains. This leaves the dependence on the particle-size ratio and the input composition, which are investigated here.

7.1. Varying the particle-size ratio

To change the particle-size ratio $R = d^l/d^s$, the particle sizes need to be changed. As a result, the local volume-fraction-weighted average particle size $\bar{d}$, defined in (5.4), also changes, and this in turn affects the segregation-velocity magnitude (5.9). To minimize this secondary effect, the particle sizes are changed in such a way that the mean inflow particle diameter $\bar{d}_{in} = \bar{\phi}_{in}^l d^l + \bar{\phi}_{in}^s d^s = 0.45$ mm. This is the same value as that used in the simulations of the self-channelized flow in §§ 3 and 4, as well as for the small-particle concentration in § 6. The values of the particle diameters used in this section are summarized in table 4.

Figure 15 shows the concentration distribution on the centreline $y = 0$ and on the plane $\xi = 0.1$ m for four values of the grain-size ratio R. The case $R = 1.49$ is the same as in § 6 and serves as a benchmark for comparison. Figure 15(a–d) show that as the grain-size ratio is decreased, the breaking-size-segregation wave becomes progressively longer and extends further upstream. In addition, the swirl of large particles that wraps around the central eye of small particles, develops a more noticeable structure. Note that when $R = 1.23$, the back of the breaking-size segregation wave extends out of the plotted domain in figure 15(d), but it is still within the computational domain $\xi \in [-0.4, 0.8]$ m. Figure 15(e,f), show that when R is decreased from 1.63 to 1.49, the width of the swirl of large grains that gets partially deposited in the levee core widens, and develops more structure. This is also true for $R = 1.36$ and $R = 1.23$, but it can not solely be deduced from figure 15(g,h), because the sections at $\xi = 0.1$ m also cut across the back of the breaking-size segregation wave in the central channel. This widening of the partially deposited breaking-size-segregation waves implies that when R is decreased, there are more fine grains in the levee core.

Movies 6–8 show the full temporal evolution of the solution for the cases $R = 1.63$, 1.36 and 1.23, using the same format as movie 2 for $R = 1.49$. The surface layer of large particles still reaches the flow front at approximately $\tau = 10$ s. However, as R decreases, it takes longer for the large particles that are overrun to segregate upwards and then recirculate towards the front again. The time to reach steady state therefore increases, from approximately 50 s for the case $R = 1.63$ to 90 s for the case $R = 1.23$.
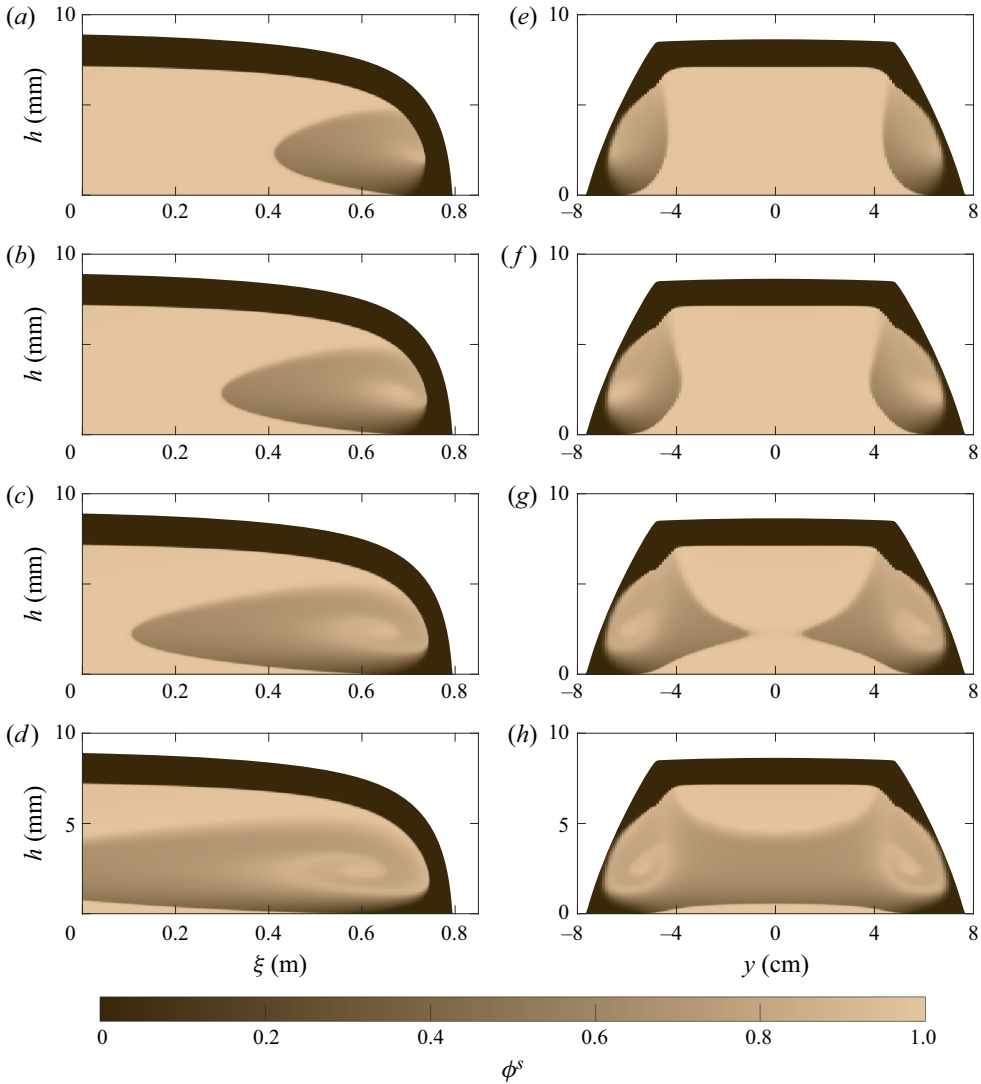
Figure 15. Colour maps of the small particle concentration ϕ^s at time $\tau = 100$ s with $\bar{\phi}_{in}^s = 0.8$ and for particle-size ratios (*a,e*) $R = 1.63$, (*b,f*) $R = 1.49$, (*c,g*) $R = 1.36$, (*d,h*) $R = 1.23$. The average particle diameter at the inflow $\bar{d}_{in} = 0.45$ mm. This constrains the particle diameters, which are summarized in table 4. Panels (*a–d*) show the $y = 0$ centre plane, while panels (*e–h*) show the cross-section at $\xi = 0.1$ m. The complete temporal evolution for $R = 1.63$, 1.36 and 1.23 are shown in movies 6–8. The case $R = 1.49$ is the same as that in §6.

7.2. *Varying the inflow concentration*

The inflow concentration $\bar{\phi}_{in}^s$ is now varied, whereas the particle sizes and hence the particle-size ratio are held fixed at the same values as §6. Figure 16 shows three new cases, for $\bar{\phi}_{in}^s = 0.9$, 0.7 and 0.6, respectively, as well as the existing case of $\bar{\phi}_s^{in} = 0.8$ as a benchmark for comparison. As $\bar{\phi}_{in}^s$ is decreased, the interface $z = \bar{\phi}_{in}^s h$ between the large and small particles at the inflow reduces in height, and the incoming layer of large particles gets thicker. Since the inflowing particles are inversely graded, they do not segregate and are simply transported by the bulk flow towards the front. The primary effect of reducing
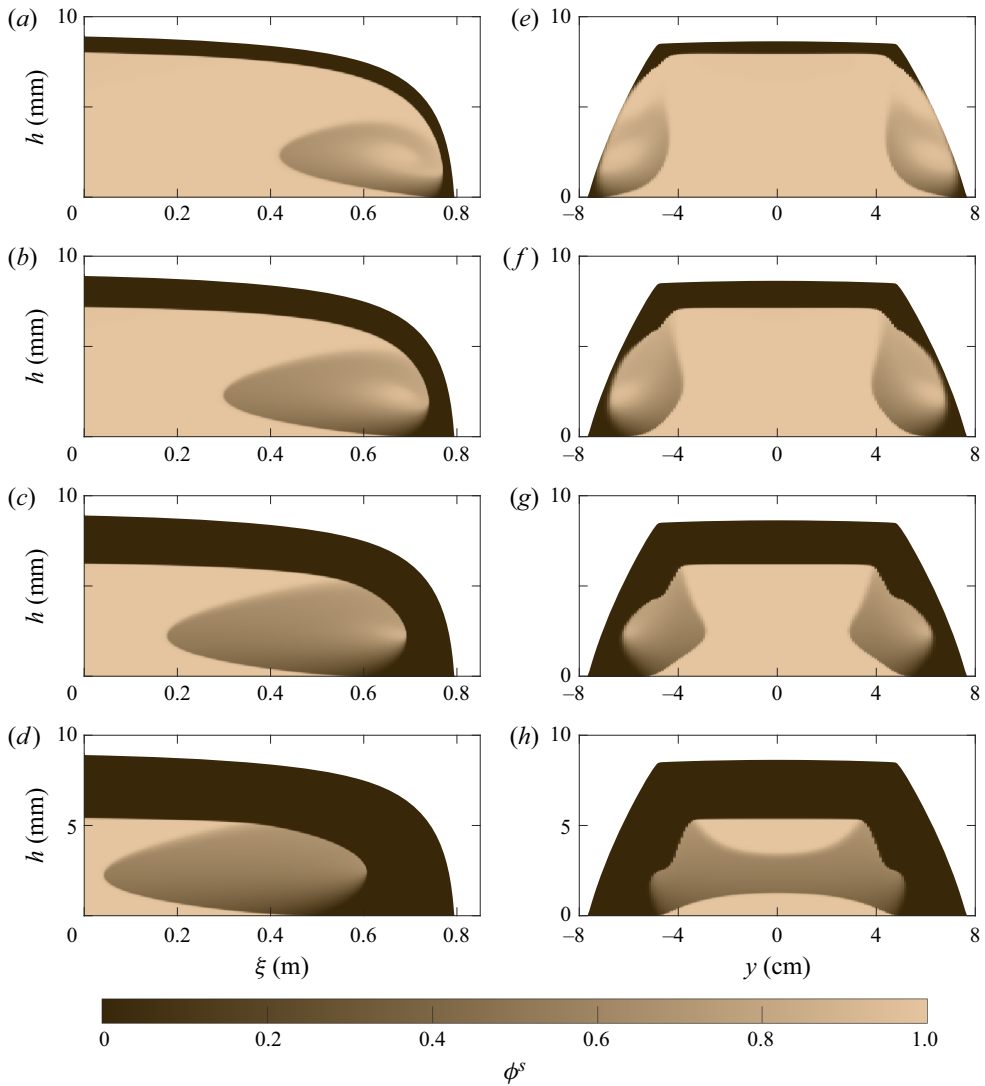
Figure 16. Colour maps of the small particle concentration ϕ^s at time $\tau = 100$ s for depth-averaged small-particle inflow concentrations (a,e) $\bar{\phi}^s_{in} = 0.9$, (b,f) $\bar{\phi}^s_{in} = 0.8$, (c,g) $\bar{\phi}^s_{in} = 0.7$, (d,h) $\bar{\phi}^s_{in} = 0.6$. The particle diameters are $d^l = 0.61$ mm and $d^s = 0.41$ mm, which corresponds to a particle-size ratio $R = 1.49$. Panels $(a$–$d)$ show the $y = 0$ centre plane, whereas panels $(e$–$h)$ show the cross-section at $\xi = 0.1$ m. The complete temporal evolution for $\bar{\phi}^s_{in} = 0.9$, 0.7 and 0.6 are shown in movies 9–11. The case $\bar{\phi}^{in}_s = 0.8$ is the same as that in § 6.

the inflow concentration is therefore to increase the thickness of the layer of large particles that develops at the free surface, as shown in figure 16(a,d). These large particles are then either advected and deposited onto the top of the levee to form a carapace, or overrun and recirculated before being deposited internally within the levees.

For the case $\bar{\phi}^s_{in} = 0.9$, the surface carapace of large particles on the levee walls gets very thin. As a result, the steady-state depth-integrated concentration (movie 9) has alternating bands of large/fine/large/fine material parallel to the downslope direction as one moves inwards from the levee margins towards the centre of the channel. These bands are due to

the fact that a significant amount of large material that was in the breaking-size-segregation wave gets trapped close to the inner margin of the levee wall, and the carapace of large grains is thicker at both the levee margin and close to the interface between the levee and the central channel. This effect can also be seen for the original simulation in figures 10 and 11 for $\bar{\phi}_{in}^s = 0.8$ with $R = 1.49$ and movie 2, but seems less pronounced. It is also evident in movie 7, but is a weak effect in the other movies.

Movies 9–11 show the temporal evolution for the cases $\bar{\phi}_{in}^s = 0.9$, 0.7 and 0.6. Once the large particles pass over the front at approximately $\tau = 10$ s again, a breaking-size-segregation wave forms. As $\bar{\phi}_{in}^s$ decreases, there are more large particles that are overrun at the front, and the breaking wave is consequently richer in large particles, and the low concentration eye of fine grains diminishes in size and appears to move towards the front of the wave. Due to the increased thickness of the free-surface layer of large particles, the breaking size segregation wave gets shifted progressively upslope as $\bar{\phi}_{in}^s$ is reduced. The length of the breaking-size-segregation wave increases as the proportion of large grains is increased, but the change in length is not as strong as the dependence on the size ratio R. This reflects the fact that although the segregation-velocity magnitude increases with increasing local mean particle diameter $\bar{d} = \phi^l d^l + \phi^s d^s$, the normal component of the large particle segregation velocity (6.9a–c) decreases with increasing large particle concentration.

The increased depth of the incoming layer of large particles at the free surface also increases the thickness of the carapace of large particles that flows out of the domain at the sides of the main channel and in the cross-sections of the levees shown in figure 16(e–h). As the small-particle concentration $\bar{\phi}_{in}^s$ is decreased, the mixed central core in the levee wall diminishes in size and the levees become almost entirely composed of large particles (figure 16h). This imposes a limit on the ability of self-channelized flows to transport the incoming mixture in a steady manner. If there are too many large particles, they cannot be accommodated in the levee walls or in the narrow boundary layers on either side of the no-net-flow line (in the central moving channel) and instead, large particles will continue to accumulate at the flow front, as in the solutions of Gray & Ancey (2009) and Gray & Kokelaar (2010).

8. Conclusions

This paper uses the depth-averaged theory of Rocha *et al.* (2019) to solve for a two-dimensional travelling wave that propagates steadily downslope and self-channelizes a flow of monodisperse dry grains. Material in the central channel is continuously transported to the flow front, where it spreads laterally and emplaces a pair of static levees just behind the front. These levees are responsible for the self-channelization of the flow, as shown in figures 3 and 4, as well as movie 1. Importantly, this theory does not rely on particle-size segregation to explain the creation of static levees. Instead, it relies on (i) frictional hysteresis (Pouliquen & Forterre 2002; Félix & Thomas 2004; Deboeuf *et al.* 2006; Mangeney *et al.* 2007; Edwards & Gray 2015; Edwards *et al.* 2017, 2019) and (ii) depth-averaged in-plane viscous stresses (Gray & Edwards 2014; Baker *et al.* 2016a). Frictional hysteresis allows static and flowing layers to coexist under the same flow conditions and, importantly, the higher-order gradient viscous terms allow a non-uniform velocity profile to develop across the central channel, providing a mechanism that determines the channel width.

Rocha *et al.* (2019) demonstrated that their theory was in quantitative agreement with small-scale experimental measurements of the variation in channel height and width, with changing mass flux (Félix & Thomas 2004; Takagi *et al.* 2011). The theory is also relevant

for large-scale geophysical flows. This is because Kokelaar *et al.* (2017) showed that the equations scale with a typical particle size. Large-scale geophysical flows of rocky regolith on the Moon are therefore mathematically equivalent, and may in reality be closely similar to small-scale experiments with approximately millimetre-scale grains (Pouliquen *et al.* 1997; Woodhouse *et al.* 2012; Baker *et al.* 2016*b*). This argument is reprised here, in § 2.4, to show that this is also true for Rocha *et al.*'s (2019) model with the full complexity of the non-monotonic friction law, defined in § 2.2, and the depth-averaged viscous terms. The solutions shown here are therefore relevant for large-scale levee-channelled flows, even those, such as debris flows and dense pyroclastic avalanches, that contain interstitial fluid. The fluid significantly reduces the apparent friction, but the resulting velocity field and flow morphology may nonetheless be very similar to that of dry flows. Here, a dry granular flow is chosen that is qualitatively similar to large-scale fluid-saturated flows at the USGS debris-flow flume (Johnson *et al.* 2012).

To solve for the evolving particle-size distribution in a self-channelized flow, it is necessary to reconstruct the three-dimensional velocity field from the two-dimensional depth-averaged one computed in § 3. This is done in § 4 by assuming Bagnold down- and cross-slope velocity profiles (4.1) and (4.2) through the flow depth, and then using the bulk incompressibility to infer the normal velocity component. The resulting three-dimensional velocity field, shown in figures 5–7, is qualitatively similar in any self-channelized flow that continuously forms static levees, whatever the context.

Geophysical mass flows contain a very wide range of particle sizes, and trying to resolve the full complexity of these distributions is difficult. However, considerable insights into where larger and smaller grains accumulate can be obtained by using a simple bidisperse theory. This paper uses the generalized bidisperse segregation model of Gray (2018) and Barker *et al.* (2021), with the empirical segregation law of Trewhela *et al.* (2021). This combined model also scales with a typical particle size, as shown in § 5.3, i.e. large boulders and smaller rocks in geophysical mass flows will segregate from one another in a similar manner to millimetre-sized grains in small-scale experiments. This makes the computations of the small-particle size distribution, shown in figures 10 and 12, as well as movie 2, pertinent for both geophysical flows and small-scale experiments.

The solutions are performed in a moving frame of reference, which moves with the speed of the flow front. Initially, the flow is assumed to be entirely composed of small particles. A pre-segregated layer of large particles is then fed into the domain across the upstream boundary. The upstream boundary condition is complicated, because large and small particles flow into the domain above the no-net-flow line (figure 9), pass through the downstream flow and eventually exit below the no-net-flow line. The three-dimensional large and small particle trajectories are visualized in figure 13 and movies 4–5. These trajectories provide a mapping between the inflow and outflow positions, above and below the no-net-flow line. A colour coded mapping for both large and small particles is shown in figure 14.

Large particles at the surface of the flow, and in the centre of the channel, are sheared towards the front where they are overrun by the bulk flow. They are, however, able to segregate upwards again in a breaking-size-segregation wave (Thornton & Gray 2008; Gray & Ancey 2009; Gray & Kokelaar 2010; Johnson *et al.* 2012; Barker *et al.* 2021), which forms just behind the large-rich front. This wave moves at the same speed as the front, and enables large grains to rise up into faster regions of the flow. The large particles that are overrun are therefore recirculated forwards again by the bulk flow, and are simultaneously pushed laterally to form looping trajectories in figure 13(*b*). Most of these large grains eventually get deposited in a mixed region within the central levee core. In the travelling

frame of reference, these deposited large grains appear to move upstream out of the flow domain. In reality, all the grains that get deposited in the levees are static.

Large particles that start closer to the sides of the central flowing channel, do not reach the front, and are pushed laterally aside, before being partially overrun, to form a carapace of large grains that covers the exterior surface and base of the levees. This is precisely what was observed in the resin-impregnated sections by Kokelaar *et al.* (2014). Small particles, however, segregate down towards the base of the flow, and either get deposited into a mixed region in the levee core or are recirculated away from the front near the base. This is due to the base of the central channel moving slower than the front speed. As a result, the small grains provide a sheared low friction internal channel lining, just as Kokelaar *et al.* (2014) observed. In fully coupled computations, this would feedback on the bulk flow by increasing the downslope velocity in the channel (Barker *et al.* 2021), although this is not resolved in the computations presented here. It does, however, confirm that particle-size segregation in self-channelized flows automatically lines the channels with low friction material, which provides a secondary mechanism for run-out enhancement (Kokelaar *et al.* 2014).

Some large particles are not deposited in the levees, but remain in the central channel. These large particles are concentrated in the boundary layers on either side of the no-net-flow line (figure 9). In these regions, the shear rate is lower than in the centre of the channel, vanishingly so at the channel/levee margins, so the large particles segregate very slowly towards the surface. Steady-state small-particle concentration solutions would therefore require a semi-infinite domain to fully resolve the steady-state solution. The computations performed here are in a finite domain, so a small proportion of the large particles exit the back of the domain within the main channel in a mixed, or not fully segregated, state. For these particles, segregation will continue further upstream, and given an infinite domain, they would segregate completely to form an inversely graded layer adjacent to the free surface. Of these mixed large particles, there is an even smaller proportion that lie beneath a region of small grains that are being sheared forwards, toward the front (above the no-net-flow line). Continued upstream segregation would allow these large particles to recirculate forwards again. Steady states are therefore weakly domain-size dependent. However, quasi-steady conditions are only ever realized in geophysical mass flows for short periods of time, so solving on a finite domain is more realistic than trying to consider a semi-infinite avalanche.

The particle-size distributions and particle paths in figures 9–16 show how large and small particles are transported, recirculated and deposited during sustained inflow. In reality, the flow will eventually wane and stop, which leads to partial draining of the channel (Félix & Thomas 2004; Johnson *et al.* 2012; Woodhouse *et al.* 2012; Rocha *et al.* 2019). Much of the material that lies above the no-net-flow line in figure 14 will therefore drain out to leave a layer of material close to h_{stop} between the levee walls, which themselves may also partially collapse. After the flow has ceased, the levees will therefore be higher than the material in the central channel, rather than having the approximately trapezoidal cross-section shown in figure 14. It is possible to capture this partial drainage with the same depth-averaged model used here (see figures 14 and 15, and movies 5 and 6 of Rocha *et al.* 2019). In principle, the same reconstruction method can be used to determine the evolving three-dimensional velocity field $\boldsymbol{u}$, and hence simultaneously solve the segregation equation (5.2) for the particle-size distribution during the flow and within the eventual deposit. This remains a significant challenge for the future, but it is this partially drained deposit that geologists and geophysicists observe in the field (see e.g. figure 2*b*).

The simple bidisperse theory used in this paper provides considerable insight into the structure of the levees and the central channel. Particle-size segregation, combined with the self-channelization wave that emplaces the levees, leads to the flow front and the levee walls being rich in large grains, while small particles are concentrated at the base of the channel and the internal levee walls. Although the current theory ignores diffusive effects, the central levee core is deposited in an arrested mixed state of large and small grains. In debris flows, this overall structure naturally leads to strong differential fluidization. Regions of large particles rapidly dissipate pore pressure and lose mobility (Iverson & Vallance 2001; Iverson 2003), which generates highly frictional flow fronts and stronger levees. However, this paper shows that it is not necessarily differential fluidization that leads to self-channelization itself. Instead, the scaling arguments, in § 2.4, show that frictional hysteresis is a plausible mechanism for self-channelization and levee formation at geophysical scale. Particle-size segregation in combination with the $\mu(I)$ rheology does however support the hypotheses that the large-rich levees are stronger, and the fines lining in the central channel enhances the flow mobility (Kokelaar *et al.* 2014). Particle-size segregation is therefore an important effect that promotes self-channelization, and should more generally be resolved in geophysical mass flow models.

Author ORCIDs.
- A.N. Edwards https://orcid.org/0000-0002-2374-0162;
- F.M. Rocha https://orcid.org/0000-0002-6522-7703;
- B.P. Kokelaar https://orcid.org/0000-0002-2452-703X;
- C.G. Johnson https://orcid.org/0000-0003-2192-3616;
- J.M.N.T. Gray https://orcid.org/0000-0003-3554-0499.

Appendix A. Well balancing of the three-dimensional velocity field

The method of Kurganov & Tadmor (2000) divides the domain into a three-dimensional grid of cuboidal finite volume cells of size $\Delta\xi \times \Delta y \times \Delta z$ and indexed by integer coordinates (i, j, k). If the central point of a grid cell is within the flow domain ($0 \leqslant z \leqslant h(\xi, y)$), then the entirety of that cell is designated to be within the flow, with all other cells designated as being outside the flow.

Within each grid cell in the flow domain, the volume average of the small particle concentration ϕ^s evolves through fluxes evaluated on the six faces surrounding a grid cell. These fluxes depend on the advection velocity field $\boldsymbol{u}'$, and require the average of the velocity component u' to be specified on each of the two faces normal to the ξ-axis, and likewise the average of v' and w' components on the faces normal to the y- and z-axes. An approximation to these velocity components, which are denoted u^a, v^a, w^a, is obtained by evaluating (4.3), (4.4) and (4.6) at the centre of each face, except at faces separating a cell inside the flow from one outside, at which the velocity component is set to zero. Specifically, $u^a_{i+1/2,j,k}$ represents this approximate u'-component of the velocity on the

face separating grid cells with indices (i, j, k) and $(i + 1, j, k)$, with $v^a_{i,j+1/2,k}$ and $w^a_{i,j,k+1/2}$ similarly defined on appropriate faces.

Numerical solutions to the segregation equation (5.17) are obtained using corrected velocity components, u^c, v^c, w^c, defined by

$$u^c = u^a + \breve{u}, \quad v^c = v^a + \breve{v}, \quad w^c = w^a + \breve{w}. \tag{A1a–c}$$

At each cell within the flow domain, a spatial discretization of (5.17) using the semi-discrete form of Kurganov & Tadmor (2000) preserves the uniform states $\phi^s = 0$ and $\phi^s = 1$ exactly only when the corrected velocities satisfy a discretized divergence-free condition,

$$\frac{u^c_{i+1/2,j,k} - u^c_{i-1/2,j,k}}{\Delta x} + \frac{v^c_{i,j+1/2,k} - v^c_{i,j-1/2,k}}{\Delta y} + \frac{w^c_{i,j,k+1/2} - w^c_{i,j,k-1/2}}{\Delta z} = 0. \tag{A2}$$

Corrections $\breve{\boldsymbol{u}} = (\breve{u}, \breve{v}, \breve{w})$ are found below, such that (A2) is satisfied exactly.

Because $\boldsymbol{u}'$ is constructed to be divergence free in (4.6), the divergence-free condition (A2) is satisfied approximately even by the uncorrected velocity $\boldsymbol{u}^a$. The divergence errors in the uncorrected velocity arise for three reasons: (*a*) a small divergence of the depth-integrated flux $h\bar{\boldsymbol{u}}$ due to small errors in the numerical solution of these fields; (*b*) the approximation of the average $\boldsymbol{u}'$ on a cell face by its value at the centre of this face; and (*c*) the approximation of the flow boundary $z = h$ by axis-aligned cell faces.

To eliminate these errors in the corrected velocity field $\boldsymbol{u}^c$, a potential $\Psi_{i,j,k}$ is defined at the centre of each grid cell, and the velocity corrections $\breve{u}$, $\breve{v}$, $\breve{w}$ at the centre of each grid face are written in terms of Ψ

$$\breve{u}_{i+1/2,j,k} = \frac{\Psi_{i+1,j,k} - \Psi_{i,j,k}}{\Delta x}, \quad \breve{v}_{i,j+1/2,k} = \frac{\Psi_{i,j+1,k} - \Psi_{i,j,k}}{\Delta y},$$

$$\breve{w}_{i,j,k+1/2} = \frac{\Psi_{i,j,k+1} - \Psi_{i,j,k}}{\Delta z}, \tag{A3a–c}$$

at interior faces, and $\breve{u}$, $\breve{v}$, $\breve{w}$ are set to zero at faces on the boundary of the flow domain.

Substituting (A1a–c) and (A3a–c) into (A2) gives a linear equation for the unknowns $\Psi_{i,j,k}$ at every grid cell, which for interior cells is

$$\frac{\Psi_{i+1,j,k} - 2\Psi_{i,j,k} + \Psi_{i-1,j,k}}{(\Delta x)^2} + \frac{\Psi_{i,j+1,k} - 2\Psi_{i,j,k} + \Psi_{i,j-1,k}}{(\Delta y)^2} + \frac{\Psi_{i,j,k+1} - 2\Psi_{i,j,k} + \Psi_{i,j,k-1}}{(\Delta z)^2}$$

$$= -\left(\frac{u^a_{i+1/2,j,k} - u^a_{i-1/2,j,k}}{\Delta x} + \frac{v^a_{i,j+1/2,k} - v^a_{i,j-1/2,k}}{\Delta y} + \frac{w^a_{i,j,k+1/2} - w^a_{i,j,k-1/2}}{\Delta z} \right). \tag{A4}$$

This discretized Poisson equation is applied at all except one of the grid cells within the flow domain, with the final equation in the linear system being that $\Psi = 0$ in the single (arbitrarily chosen) remaining grid cell. Summing (A2) over every grid cell in the solution domain reveals that (A2) can be satisfied also in the grid cell where $\Psi = 0$ is set by choosing the frame speed such that the sum of the fluxes across the back of the flow domain $\xi = -0.4$ m is zero. This gives a slightly modified front velocity $u_F = 0.07058$ m s^{-1}.

A solution for $\Psi_{i,j,k}$ is required at every interior flow point, which number approximately 4×10^7. The resulting large linear system is solved using the preconditioned conjugate gradient method with a diagonal preconditioner, and the corrected velocity field obtained through (A3a–c)–(A1a–c). This procedure produces a corrected velocity field $\boldsymbol{u}^c$ that is

very similar to the uncorrected one, but with a numerical divergence (and consequent 'drift' in steady solutions of ϕ^s) reduced by a factor of $\sim 10^8$. The remaining, negligible, divergence error arises from truncation error and a finite convergence tolerance for the iterative linear solver.

This correction can be thought of as a discrete analogue of the Helmholtz decomposition, in which the prescribed velocity field is decomposed into curl-free and divergence-free components, and the small curl-free component subtracted off to leave only the divergence-free component of the original field.

REFERENCES

ANCEY, C. 2012 Are there 'dragon-kings' events (i.e. genuine outliers) among extreme avalanches? *Eur. Phys. J.: Spec. Top.* **205**, 117–129.

BAKER, J., BARKER, T. & GRAY, J.M.N.T. 2016a A two-dimensional depth-averaged $\mu(I)$-rheology for dense granular avalanches. *J. Fluid. Mech.* **787**, 367–395.

BAKER, J., JOHNSON, C.G. & GRAY, J.M.N.T. 2016b Segregation-induced finger formation in granular free-surface flows. *J. Fluid Mech.* **809**, 168–212.

BARKER, T. & GRAY, J.M.N.T. 2017 Partial regularisation of the incompressible $\mu(I)$-rheology for granular flow. *J. Fluid Mech.* **828**, 5–32.

BARKER, T., RAUTER, M., MAGUIRE, E.S.F., JOHNSON, C.G. & GRAY, J.M.N.T. 2021 Coupling rheology and segregation in granular flows. *J. Fluid Mech.* **909**, A22.

BARKER, T., SCHAEFFER, D.G., BOHÓRQUEZ, P. & GRAY, J.M.N.T. 2015 Well-posed and ill-posed behaviour of the $\mu(I)$-rheology for granular flows. *J. Fluid. Mech.* **779**, 794–818.

BARTELT, P., GLOVER, J., FEISTL, T., BÜHLER, Y. & BUSER, O. 2012 Formation of levees and en-echelon shear planes during snow avalanche run-out. *J. Glaciol.* **58**, 980–992.

BOUZID, M., IZZET, A., TRULSSON, M., CLÉMENT, E., CLAUDIN, P. & ANDREOTTI, B. 2015 Non-local rheology in dense granular flows: revisiting the concept of fluidity. *Eur. Phys. J.* E **38**, 125.

BOUZID, M., TRULSSON, M., CLAUDIN, P., CLÉMENT, E. & ANDREOTTI, B. 2013 Nonlocal rheology of granular flows across yield conditions. *Phys. Rev. Lett.* **111** (23), 238301.

BOYER, F., GUAZZELLI, E. & POULIQUEN, O. 2011 Unifying suspension and granular rheology. *Phys. Rev. Lett.* **107**, 188301.

BRANNEY, M.J. & KOKELAAR, B.P. 1992 A reappraisal of ignimbrite emplacement: progressive aggradation and changes from particulate to non-particulate flow during emplacement of high-grade ignimbrite. *Bull. Volcanol.* **54**, 504–520.

CALDER, E.S., SPARKS, R.S.J. & GARDEWEG, M.C. 2000 Erosion, transport and segregation of pumice and lithic clasts in pyroclastic flows inferred from ignimbrite at lascar volcano, chile. *J. Volcanol. Geotherm. Res.* **104**, 201–235.

COSTA, J.E. & WILLIAMS, G. 1984 Debris flow dynamics. *Tech. Rep.* 84-606. videotape U.S. Geological Survey.

DAERR, A. & DOUADY, S. 1999 Two types of avalanche behaviour in granular media. *Nature* **399**, 241–243.

DEBOEUF, S., LAJEUNESSE, E., DAUCHOT, O. & ANDREOTTI, B. 2006 Flow rule, self channelization, and levees in unconfined granular flows. *Phys. Rev. Lett.* **97**, 158303.

DENISSEN, I.F.C., WEINHART, T., TE VOORTWIS, A., LUDING, S., GRAY, J.M.N.T. & THORNTON, A.R. 2019 Bulbous head formation in bidisperse shallow granular flow over an inclined plane. *J. Fluid Mech.* **866**, 263–297.

DENLINGER, R.P. & IVERSON, R.M. 2001 Flow of variably fluidized granular masses across three-dimensional terrain 2. Numerical predictions and experimental tests. *J. Geophys. Res.* **106** (B1), 553–566.

EDWARDS, A.N. & GRAY, J.M.N.T. 2015 Erosion-deposition waves in shallow granular free-surface flows. *J. Fluid Mech.* **762**, 35–67.

EDWARDS, A.N., RUSSELL, A.S., JOHNSON, C.G. & GRAY, J.M.N.T. 2019 Frictional hysteresis and particle deposition in granular free-surface flows. *J. Fluid Mech.* **875**, 1058–1095.

EDWARDS, A.N., VIROULET, S., KOKELAAR, B.P. & GRAY, J.M.N.T. 2017 Formation of levees, troughs and elevated channels by avalanches on erodible slopes. *J. Fluid Mech.* **823**, 278–315.

FAN, Y., SCHLICK, C.P., UMBANHOWAR, P.B., OTTINO, J.M. & LUEPTOW, R.M. 2014 Modelling size segregation of granular materials: the roles of segregation, advection and diffusion. *J. Fluid Mech.* **741**, 252–279.

FÉLIX, G. & THOMAS, N. 2004 Relation between dry granular flow regimes and morphology of deposits: formation of levées in pyroclastic deposits. *Earth Planet. Sci. Lett.* **221**, 197–213.

FORTERRE, Y. & POULIQUEN, O. 2003 Long-surface-wave instability dense granular flows. *J. Fluid Mech.* **486**, 21–50.

FRY, A.M., UMBANHOWAR, P.B., OTTINO, J.M. & LUEPTOW, R.M. 2019 Diffusion, mixing, and segregation in confined granular flows. *AIChE J.* **65**, 875–881.

GDRMIDI 2004 On dense granular flows. *Eur. Phys. J.* E **14**, 341–365.

GEORGE, D.L. & IVERSON, R.M. 2014 A depth-averaged debris-flow model that includes the effects of evolving dilatancy. II. Numerical predictions and experimental tests. *Proc. R. Soc. Lond.* A **470**, 1–31.

GOLICK, L.A. & DANIELS, K.E. 2009 Mixing and segregation rates in sheared granular materials. *Phys. Rev.* E **80** (4), 042301.

GOUJON, C., DALLOZ-DUBRUJEAUD, B. & THOMAS, N. 2007 Bidisperse granular avalanches on inclined planes: a rich variety of behaviours. *Eur. Phys. J.* E **23**, 199–215.

GRAY, J.M.N.T. 2018 Particle segregation in dense granular flows. *Annu. Rev. Fluid Mech.* **50**, 407–433.

GRAY, J.M.N.T. & ANCEY, C. 2009 Segregation, recirculation and deposition of coarse particles near two-dimensional avalanche fronts. *J. Fluid Mech.* **629**, 387–423.

GRAY, J.M.N.T. & ANCEY, C. 2011 Multi-component particle size-segregation in shallow granular avalanches. *J. Fluid Mech.* **678**, 535–588.

GRAY, J.M.N.T. & CHUGUNOV, V.A. 2006 Particle-size segregation and diffusive remixing in shallow granular avalanches. *J. Fluid Mech.* **569**, 365–398.

GRAY, J.M.N.T. & EDWARDS, A.N. 2014 A depth-averaged $\mu(I)$-rheology for shallow granular free-surface flows. *J. Fluid Mech.* **755**, 503–544.

GRAY, J.M.N.T. & KOKELAAR, B.P. 2010 Large particle segregation, transport and accumulation in granular free-surface flows. *J. Fluid Mech.* **652**, 105–137.

GRAY, J.M.N.T. & THORNTON, A.R. 2005 A theory for particle size segregation in shallow granular free-surface flows. *Proc. R. Soc. Lond.* A **461**, 1447–1473.

HILL, K.M. & TAN, S.D. 2014 Segregation in dense sheared flows: gravity, temperature gradients, and stress partitioning. *J. Fluid Mech.* **756**, 54–88.

IVERSON, R.M. & GEORGE, D.L. 2014 A depth-averaged debris-flow model that includes the effects of evolving dilatancy. I. Physical basis. *Proc. R. Soc. Lond.* A **470**, 20130819.

IVERSON, R.M. 1997 The physics of debris-flows. *Rev. Geophys.* **35**, 245–296.

IVERSON, R.M. 2003 The debris-flow rheology myth. In *Debris-Flow Hazards Mitigation: Mechanics, Prediction and Assessment* (ed. D. Rickenmann & C.L. Chen), pp. 303–314. Millpress.

IVERSON, R.M. & DENLINGER, R.P. 2001 Flow of variably fluidized granular masses across three-dimensional terrain 1. Coulomb mixture theory. *J. Geophys. Res.* **106** (B1), 553–566.

IVERSON, R.M., LOGAN, M., LaHUSEN, R.G. & BERTI, M. 2010 The perfect debris flow? Aggregated results from 28 large-scale experiments. *J. Geophys. Res.* **115**, F03005.

IVERSON, R.M. & VALLANCE, J.W. 2001 New views of granular mass flows. *Geology* **29** (2), 115–118.

JESSOP, D.E., KELFOUN, K., LABAZUY, P., MANGENEY, A., ROCHE, O. & TILLIER, J.-L. 2012 Lidar derived morphology of the 1993 Lascar pyroclastic flow deposits, and implication for flow dynamics and rheology. *J. Volcanol. Geotherm. Res.* **245–246** (19), 81–97.

JOHNSON, C.G., KOKELAAR, B.P., IVERSON, R.M., LOGAN, M., LaHUSEN, R.G. & GRAY, J.M.N.T. 2012 Grain-size segregation and levee formation in geophysical mass flows. *J. Geophys. Res.* **117**, F01032.

JOMELLI, V. & BERTRAN, P. 2001 Wet snow avalanche deposits in the french alps: structure and sedimentology. *Geografis. Annal.* **83**, 15–28.

JOP, P., FORTERRE, Y. & POULIQUEN, O. 2005 Crucial role of sidewalls in granular surface flows: consequences for the rheology. *J. Fluid Mech.* **541**, 167–192.

JOP, P., FORTERRE, Y. & POULIQUEN, O. 2006 A constitutive relation for dense granular flows. *Nature* **44**, 727–730.

KAMRIN, K. & HENANN, D.L. 2015 Nonlocal modeling of granular flows down inclines. *Soft Matt.* **11**, 179–185.

KAMRIN, K. & KOVAL, G. 2012 Nonlocal constitutive relation for steady granular flow. *Phys. Rev. Lett.* **108** (17), 178301.

KOKELAAR, B.P., BAHIA, R.S., JOY, K.H., VIROULET, S. & GRAY, J.M.N.T. 2017 Granular avalanches on the moon: mass-wasting conditions, processes, and features. *J. Geophys. Res.* **122**, 1893–1925.

KOKELAAR, B.P., GRAHAM, R.L., GRAY, J.M.N.T. & VALLANCE, J.W. 2014 Fine-grained linings of leveed channels facilitate runout of granular flows. *Earth Planet. Sci. Lett.* **385**, 172–180.

KURGANOV, A. & TADMOR, E. 2000 New high-resolution central schemes for nonlinear conservationl laws and convection-diffusion equations. *J. Comput. Phys.* **160**, 241–282.

LAGRÉE, P.-Y., STARON, L. & POPINET, S. 2011 The granular column collapse as a continuum: validity of a two-dimensional navier-stokes model with a $\mu(I)$-rheology. *J. Fluid Mech.* **686**, 378–408.

LAIGLE, D. & BARDOU, E. 2022 *5.05 – Mass-Movement Types and Processes: Flow-Like Mass Movements, Debris Flows and Earth Flows*, 2nd edn, vol. 5, pp. 61–84. Elsevier.

LEVEQUE, R.J. 2002 *Finite Volume Methods for Hyperbolic Problems*. Cambridge University Press.

MAJOR, J.J. 1997 Depositional processes in large-scale debris-flow experiments. *J. Geol.* **105**, 345–366.

MAJOR, J.J. & IVERSON, R.M. 1999 Debris-flow deposition: effects of pore-fluid pressure and friction concentrated at flow margins. *Geol. Soc. Am. Bull.* **111** (10), 1424–1434.

MANGENEY, A., BOUCHUT, F., THOMAS, N., VILOTTE, J.P. & BRISTEAU, M.O. 2007 Numerical modeling of self-channeling granular flows and of their levee-channel deposits. *J. Geophys. Res.* **112**, F02017.

MARKS, B., ROGNON, P. & EINAV, I. 2012 Grainsize dynamics of polydisperse granular flows down inclined planes. *J. Fluid Mech.* **690**, 499–511.

MARTIN, N., IONESCU, I.R., MANGENEY, A., BOUCHUT, F. & FARIN, M. 2017 Continuum viscoplastic simulation of a granular column collapse on large slopes: $\mu(I)$-rheology and lateral wall effects. *Phys. Fluids* **29** (1), 013301.

MAURIN, R., CHAUCHAT, J. & FREY, P. 2016 Dense granular flow rheology in turbulent bedload transport. *J. Fluid Mech.* **804**, 490–512.

MCARDELL, B.W. 2016 Field measurements of forces in debris flows at the illgraben: implications for channel-bed erosion. *Intl J. Erosion Control Engng* **9** (4), 194–198.

MENG, X., JOHNSON, C.G. & GRAY, J.M.N.T. 2022 Formation of dry granular fronts and watery tails in debris flows. *J. Fluid Mech.* **943**, A19.

MENG, X. & WANG, Y. 2016 Modelling and numerical simulation of two-phase debris flows. *Acta Geotech.* **11**, 1027–1045.

MOWLAVI, S. & KAMRIN, K. 2021 Interplay between hysteresis and nonlocality during onset and arrest of flow in granular materials. *Soft Matt.* **17**, 7359.

PELANTI, M., BOUCHUT, F. & MANGENEY, A. 2008 A Roe-type scheme for two-phase shallow granular flows over variable topography. *ESAIM: Math. Model. Num.* **42**, 851–885.

PIERSON, T.C. 1986 Flow behavior of channelized debris flows, Mount St. Helens, Washington. In *Hillslope Processes* (ed. A.D. Abrahams), pp. 269–296. Allen and Unwin.

PITMAN, E.B. & LE, L. 2005 A two-fluid model for avalanche and debris flows. *Phil. Trans. R. Soc. Lond.* A **363**, 1573–1601.

POULIQUEN, O. 1999*a* Scaling laws in granular flows down rough inclined planes. *Phys. Fluids* **11** (3), 542–548.

POULIQUEN, O. 1999*b* On the shape of granular fronts down rough inclined planes. *Phys. Fluids* **11** (7), 1956–1958.

POULIQUEN, O., DELOUR, J. & SAVAGE, S.B. 1997 Fingering in granular flows. *Nature* **386**, 816–817.

POULIQUEN, O. & FORTERRE, Y. 2002 Friction law for dense granular flows: application to the motion of a mass down a rough inclined plane. *J. Fluid Mech.* **453**, 133–151.

POULIQUEN, O. & FORTERRE, Y. 2009 A non-local rheology for dense granular flows. *Phil. Trans. R. Soc. Lond.* A **367**, 5091–5107.

PUDASAINI, S. 2012 A general two-phase debris flow model. *J. Geophys. Res.* **117**, F03010.

ROCHA, F.M., JOHNSON, C.G. & GRAY, J.M.N.T. 2019 Self-channelization and levee formation in monodisperse granular flows. *J. Fluid Mech.* **876**, 591–641.

ROGNON, P.G., ROUX, J.N., NAAIM, M. & CHEVOIR, F. 2007 Dense flows of bidisperse assemblies of disks down an inclined plane. *Phys. Fluids* **19**, 058101.

ROWLEY, P.D., KUNTZ, M.A. & MACLEOD, N.S. 1981 Pyroclastic-flow deposits. In *The 1980 Eruptions of Mount St. Helens, Washington* (ed. P.W. Lipman & D.R. Mullineaux), pp. 489–512. US Geol. Surv. Prof. Pap. 1250.

SAINGIER, G., DEBOEUF, S. & LAGRÉE, P.-Y. 2016 On the front shape of an inertial granular flow down a rough incline. *Phys. Fluids* **28**, 053302.

SCHAEFFER, D.G., BARKER, T., TSUJI, D., GREMAUD, P., SHEARER, M. & GRAY, J.M.N.T 2019 Constitutive relations for compressible granular flow in the inertial regime. *J. Fluid Mech.* **874**, 926–951.

SCHALL, P. & VAN HECKE, M. 2010 Shear bands in matter with granularity. *Annu. Rev. Fluid Mech.* **42**, 67–88.

SCHLICK, C.P., FAN, Y., UMBANHOWAR, P.B., OTTINO, J.M. & LUEPTOW, R.M. 2015 Granular segregation in circular tumblers: theoretical model and scaling laws. *J. Fluid Mech.* **765**, 632–652.

SCHWEIZER, J., BARTELT, P. & VAN HERWIJNEN, A. 2014 Snow avalanches. In *Snow and Ice-Related Hazards, Risks and Disasters* (ed. W. Haeberli & C. Whiteman), pp. 395–436. Elsevier.

SHARP, R.P. & NOBLES, L.H. 1953 Mudflow of 1941 at Wrightwood, Southern California. *Geol. Soc. Am. Bull.* **66**, 1489–1498.

SILBERT, L.E., ERTAŞ, D., GREST, G.S., HALSEY, T.C., LEVINE, D. & PLIMPTON, S.J. 2001 Granular flow down an inclined plane: Bagnold scaling and rheology. *Phys. Rev.* E **64**, 051302.

STARON, L., LAGRÉE, P.-Y. & POPINET, S. 2012 The granular silo as a continuum plastic flow: the hour-glass vs the clepsydra. *Phys. Fluids* **24**, 103301.

TAKAGI, D., McELWAINE, J.N. & HUPPERT, H.H. 2011 Shallow granular flows. *Phys. Rev.* E **83**, 031306.

TAPIA, F., ICHIHARA, M., POULIQUEN, O. & GUAZZELLI, E. 2022 Viscous to inertial transition in dense granular suspension. *Phys. Rev. Lett.* **129**, 078001.

THOMAS, N. 2000 Reverse and intermediate segregation of large beads in dry granular media. *Phys. Rev.* E **62**, 961–974.

THORNTON, A.R. & GRAY, J.M.N.T. 2008 Breaking size-segregation waves and particle recirculation in granular avalanches. *J. Fluid Mech.* **596**, 261–284.

THORNTON, A.R., GRAY, J.M.N.T. & HOGG, A.J. 2006 A three-phase mixture theory for particle size segregation in shallow granular free-surface flows. *J. Fluid Mech.* **550**, 1–25.

THORNTON, A.R., WEINHART, T., LUDING, S. & BOKHOVE, O. 2012 Modeling of particle size segregation: calibration using the discrete particle method. *Intl J. Mod. Phys.* **23**, 1240014.

TREWHELA, T., ANCEY, C. & GRAY, J.M.N.T. 2021 An experimental scaling law for particle-size segregation in dense granular flows. *J. Fluid Mech.* **916**, A55.

UTTER, B. & BEHRINGER, R.P. 2004 Self-diffusion in dense granular shear flows. *Phys. Rev.* E **69**, 031308.

VAN DER VAART, K., GAJJAR, P., EPELY-CHAUVIN, G., ANDREINI, N., GRAY, J.M.N.T. & ANCEY, C. 2015 Underlying asymmetry within particle size segregation. *Phys. Rev. Lett.* **114**, 238001.

VALLANCE, J.W. 2000 Lahars. In *Encyclopedia of Volcanoes* (ed. H. Sigurdsson), pp. 601–616. Academic.

VALLANCE, J.W. & IVERSON, R.M. 2015 Lahars and their deposits. In *Encyclopedia of Volcanoes*, 2nd edn (ed. H. Sigurdsson), pp. 649–664. Elsevier.

WIEDERSEINER, S., ANDREINI, N., EPELY-CHAUVIN, G., MOSER, G., MONNEREAU, M., GRAY, J.M.N.T. & ANCEY, C. 2011 Experimental investigation into segregating granular flows down chutes. *Phys. Fluids* **23**, 013301.

WILSON, L. & HEAD, J.W. 1981 Morphology and rheology of pyroclastic flows and their deposits, and guidlines for future observations. In *The 1980 Eruptions of Mount St. Helens, Washington* (ed. P.W. Lipman & D.R. Mullineaux), pp. 513–524. US Geol. Surv. Prof. Pap. 1250.

WOODHOUSE, M.J., THORNTON, A.R., JOHNSON, C.G., KOKELAAR, B.P. & GRAY, J.M.N.T. 2012 Segregation-induced fingering instabilities in granular free-surface flows. *J. Fluid Mech.* **709**, 543–580.